

2012

Computer Simulations of Faceted Nanoparticles and Carbon Nanotubes in Liquid Crystals

Shivkumar Shankar Bale

Louisiana State University and Agricultural and Mechanical College

Follow this and additional works at: https://repository.lsu.edu/gradschool_dissertations



Part of the [Chemical Engineering Commons](#)

Recommended Citation

Bale, Shivkumar Shankar, "Computer Simulations of Faceted Nanoparticles and Carbon Nanotubes in Liquid Crystals" (2012). *LSU Doctoral Dissertations*. 645.
https://repository.lsu.edu/gradschool_dissertations/645

This Dissertation is brought to you for free and open access by the Graduate School at LSU Scholarly Repository. It has been accepted for inclusion in LSU Doctoral Dissertations by an authorized graduate school editor of LSU Scholarly Repository. For more information, please contact gradetd@lsu.edu.

COMPUTER SIMULATIONS OF FACETED NANOPARTICLES AND CARBON
NANOTUBES IN LIQUID CRYSTALS

A Dissertation

Submitted to the Graduate Faculty of the
Louisiana State University and
Agricultural and Mechanical College
in partial fulfillment of the
requirements for the degree of
Doctor in Philosophy

in

The Department of Chemical Engineering

by

Shivkumar Shankar Bale

B.Tech., Mumbai University Institute of Chemical Technology, 2006

August 2012

ACKNOWLEDGEMENTS

I owe my deepest gratitude to my advisor, Dr. Francisco Hung, for his guidance, encouragement, and support throughout my doctoral work. It has been an honor to be his first graduate student.

I would also like to thank my committee members, Dr. Bin Chen, Dr. John Flake, Dr. James Geaghan, Dr. Krishnaswamy Nanadakumar and Dr. Jose A. Romagnoli (General Exam) for taking time to evaluate my research.

I would also like to acknowledge the Louisiana Board of Regents for their funds, LONI & HPC-LSU for the computing time, Cain department of Chemical Engineering and its staff, especially Darla Dao and Melissa Fay, for their assistance with the office work and, Thilanga P. Liyana-Arachchi for his kind support.

Special thanks to my parents, Shankar and Vijaya Bale, for making me whom I am today, my younger brother, Santosh Bale, for the good times we had and my LSU roommate, Dhruva Dhavale, for making me feel at home.

TABLE OF CONTENTS

ACKNOWLEDGEMENTS.....	ii
LIST OF FIGURES	iv
ABSTRACT	vii
CHAPTER 1. INTRODUCTION.....	1
CHAPTER 2. TORQUE TRANSMITTED BY THE NEMATIC LIQUID CRYSTAL TO THE FACETED NANOPARTICLES.....	10
2.1. Models and Methods.....	10
2.1.1. Details of the Model Systems	10
2.1.2. Mesoscale Theory for the Nematic Liquid Crystal	15
2.2. Results and Discussions	19
2.2.1. Triangular Prism Shaped Particle.....	19
2.2.2. Cubic Particle	27
2.3. Concluding Remarks.....	44
CHAPTER 3. MOLECULAR DYNAMICS SIMULATION OF SYSTEMS OF CARBON NANOTUBES AND LIQUID CRYSTALS	47
3.1. Simulation Details	47
3.2. Results and Discussions	50
3.2.1. Investigating the Interactions between the CNTs in 5CB and 8CB Nematic Liquid Crystal System.....	50
3.2.2. Investigating the Interactions between the CNTs in 8CB Nematic and Smectic Liquid Crystal System.....	55
3.3. Concluding Remarks.....	61
CHAPTER 4. CONCLUSIONS AND FUTURE DIRECTIONS	63
REFERENCES	67
APPENDIX A.....	77
APPENDIX B.....	78
VITA	80

LIST OF FIGURES

Figure 1.1: Top: schematic representations of crystal, nematic liquid crystal (NLC), smectic liquid crystal (SLC) and isotropic liquid phase [38]. Bottom: different examples of the ordered structure when μm -sized particles are immersed in NLCs [4, 12].2

Figure 1.2: Three types of defect structures when a spherical particle is immersed in a LC: the dipole configuration, the Saturn ring configuration, and the surface ring configuration [52].4

Figure 2.1: Schematic representation of (a) rectangular box full of nematic liquid crystal, (b) cubic nanoparticle, and (c) equilateral triangular prism shaped nanoparticle [111].11

Figure 2.2: (a) The triangular prism particle is rotated around the two axes (1) only x axes (2) the axis passing through two diagonal vertices of two triangular faces as indicated in the figure. In all cases, far field director $n(r)$ is parallel to the z -axis. (b) The cubic nanoparticle is rotated around the five axes out of thirteen rotational symmetry axes as indicated in the figure [111].13

Figure 2.3: Total torque transmitted by the nematic liquid crystal on the one equilateral triangular prism shaped nanoparticle, rotated around the x axis, as a function of angle of rotation. The enclosed blue rectangular region represents angles with out-of-plane rotation and the enclosed green region represents angles with in-plane rotation. Circles indicate the stable and zero torque configuration.21

Figure 2.4: 3D visualizations of the NLC distortion around the equilateral triangular prism shaped particle when the particle is rotated around x axis at angle θ22

Figure 2.5: Contour map of the NLC distortion (scalar order parameter S) around the equilateral triangular prism shaped particle rotated around x axis at angle (a) $\theta = 0^\circ$ (b) $\theta = 30^\circ$ and (c) $\theta = 60^\circ$. The orientations a, b and c are symmetric, and the NLC distortion around those orientations is balanced because the scalar order parameter S near one of the three sides is similar to that of the other side. If the NLC distortion is unbalanced around the particle, the S would be different on all the three sides.23

Figure 2.6: Torque transmitted by the nematic liquid crystal on the two equilateral triangular prism shaped particle system as a function of minimum surface-to-surface interparticle distance d . Triangles: x component of torque acting over particle 1 (red) and 2 (blue). Circles: y component of torque acting over particle 1 (red) and 2 (blue). Squares: z component of torque acting over particle 1 (red) and 2 (blue).25

Figure 2.7: 3D visualizations of the NLC distortion around the two equilateral triangular prism shaped particles separated by the interparticle distance d26

Figure 2.8: Total torque transmitted by the nematic liquid crystal on the one cubic nanoparticle, rotated around the $x=y=z$ axis, as a function of angle of rotation. The enclosed blue rectangular region represents angles with out-of-plane rotation and the enclosed green region represents angles with in-plane rotation. Circle indicates the most stable and a zero torque configuration. .29

Figure 2.9: 3D visualizations of the NLC distortion around the cubic particle when the particle is rotated around $x=y=z$ axis at angle θ	30
Figure 2.10: Total torque transmitted by the nematic liquid crystal on the one cubic nanoparticle, rotated around the $x=0, y=z$ axis, as a function of angle of rotation. The enclosed blue rectangular region represents angles with out-of-plane rotation and the enclosed green region represents angles with in-plane rotation. Circle indicates the most stable and a zero torque configuration.	31
Figure 2.11: 3D visualizations of the NLC distortion around the cubic particle when the particle is rotated around $x=0, y=z$ axis at angle $\theta = 90^\circ$	32
Figure 2.12: Total torque transmitted by the nematic liquid crystal on the one cubic nanoparticle, rotated around the $z=0, x=y$ axis, as a function of angle of rotation. The enclosed light blue rectangular region represents angles with out-of-plane rotation 1, the enclosed dark blue region represents angles with out-of-plane rotation 2 and the enclosed black region represents angles with unconventional rotation. The circle indicates the zero torque configuration and the triangle indicates the most stable configuration.	34
Figure 2.13: 3D visualizations of the NLC distortion around the cubic particle when the particle is rotated around $z=0, x=y$ axis at angle θ	35
Figure 2.14: Total torque transmitted by the nematic liquid crystal on the one cubic nanoparticle, rotated around the x axis, as a function of angle of rotation. The enclosed blue rectangular region represents angles with out-of-plane rotation, the enclosed green region represents angles with in-plane rotation and the enclosed black region represents angles with unconventional rotation. Circle indicates the most stable and a zero torque configuration.	37
Figure 2.15: 3D visualizations of the NLC distortion around the cubic particle when the particle is rotated around x axis at angle θ	38
Figure 2.16: Torque transmitted by the nematic liquid crystal on the two cubic particle system as a function of minimum surface-to-surface interparticle distance d . Triangles: x component of torque acting over particle 1 (red) and 2 (blue). Circles: y component of torque acting over particle 1 (red) and 2 (blue). Squares: z component of torque acting over particle 1 (red) and 2 (blue).	41
Figure 2.17: (a) Schematic representation of two cubic particles approaching each other through the interparticle distance d . (b) 3D visualizations of the defect structure formed by a nematic liquid crystal around the two cubic particles separated by the interparticle distance $d = 4$ nm. ...	42
Figure 3.1: Representative simulation snapshot of an MD simulation of a system of two CNTs immersed in 5CB in the nematic phase.	48
Figure 3.2: The molecular structure of 5CB and 8CB LC. 8CB LC has three more carbon atoms in the hydrophobic part of the molecule than 5CB LC.	49

Figure 3.3: The calculated PMF, for the system of CNTs immersed in the 5CB and 8CB NLCs, as a function of the fixed distance d between the CNTs.52

Figure 3.4: Number of hydrophobic (HO) and hydrophilic (HI) atoms of 5CB and 8CB NLCs in the volume between the CNTs, as a function of fixed distance d53

Figure 3.5: The calculated PMF, for the system of CNTs immersed in the 8CB NLCs and SLCs, as a function of the fixed distance d between the CNTs.57

Figure 3.6: Number of hydrophobic (HO) and hydrophilic (HI) atoms of 8CB NLCs and SLCs in the volume between the CNTs, as a function of fixed distance d58

Figure 3.7: The simulation snapshot of (a) CM, (b) DM (c) SSM (d) SDM and (e) TM configuration for a system of two CNTs immersed in the 8CB SLCs.....59

Figure 3.8: Front view of the simulation snapshot of (a) DM and (b) SDM configuration for a system of two CNTs immersed in the 8CB SLCs.....60

ABSTRACT

The purpose of this research is to investigate the use of liquid crystals (LCs) to manipulate and organize faceted nanoparticles and carbon nanotubes (CNTs). Computer simulations at different levels of detail are used to study these systems. Results from this project will be relevant for potential applications of these systems in displays, nanoscale electronics, electro-optical switches, and in the development of composites with unique mechanical, thermal and/or electronic properties.

In this research, two independent but directly related projects were carried out. In the first part of the research, we investigated the torque that develops when faceted nanoparticles, namely cubes and triangular prisms, are immersed in a nematic LC. We used a mesoscale theory in terms of the tensor order parameter $\mathbf{Q}(\mathbf{r})$ to model the nematic. Homeotropic anchoring condition of the NLC is imposed on the surfaces of faceted nanoparticles. Our results indicate that, when the particle is oriented at an out-of-plane orientation (i.e. unstable configuration), it moves away immediately from that state and then slowly orients itself back to the stable configuration (i.e. in-plane orientation). The magnitude of the out-of-plane torques is similar to that of in-plane torques. In case of an isolated nanoprism system, the torque reaches maximum when the particle orients with one of its rectangular sides parallel to the far field director $\mathbf{n}(\mathbf{r})$. In contrast, the torque of an isolated nanocube system reaches maximum when the particle orients with its four lateral faces parallel to the far field director $\mathbf{n}(\mathbf{r})$. In the second part of our research, we investigated the effect of varying the molecular structure and the phase of the LC on the CNTs interactions by performing MD simulations. Our results suggest that increasing the chain length of the hydrophobic tail of the nCB LC molecule decreases the tendency of aggregation for CNTs in nCB LCs. Additionally, varying the phase of the nCB LC is insufficient to decrease the tendency of aggregation for CNTs.

CHAPTER 1. INTRODUCTION

Liquid crystals (LCs) exhibit properties common to those observed in an isotropic liquid and a 3D ordered crystal (Figure 1.1). Thermotropic LCs, which typically consist of anisotropic molecules (e.g., rod-like shaped), exhibit orientational order in which most of the molecules are pointing in the same direction, as in a 3D crystal phase; however, a LC can flow, in analogy to an isotropic liquid phase. A common LC phase is a nematic liquid crystal (NLC), which exhibits orientational order and positional disorder (Figure 1.1). In a LC, the director field $\mathbf{n}(\mathbf{r})$ indicates the average orientation of the molecules at a given position \mathbf{r} . Electric and magnetic fields, flows and external surfaces can be used to modify the alignment of the director field, with time responses on the order of milliseconds. These principles form the basis of modern LC-display devices.

Systems of particles immersed in LCs have attracted attention for the development of composite and structured materials. When the particles are introduced in the LC, they produce a distortion in its director field. Thus the particles and the LC will try to minimize the elastic perturbation, which leads to long range interparticle interactions. These interactions can induce the formation of a number of ordered colloid structures [1-17] and depends on the shape and size of the particles, the local anchoring of the LC at the surface of the colloids, the alignment of the director field far away from the particles, and the geometry of the surrounding. According to recent experiments [1-4, 7-10, 12-18] and calculations [9, 10, 12-17, 19-24], long-range interparticle interactions are anisotropic and can be strong (several thousands of $k_B T$). Most of the above experimental work has considered systems of spherical, micron sized particles in LC; however, a number of experimental studies have also worked on spherical [25-30] or rod-like nanoparticles [31-37] in LC. These systems have potential applications in light-scattering

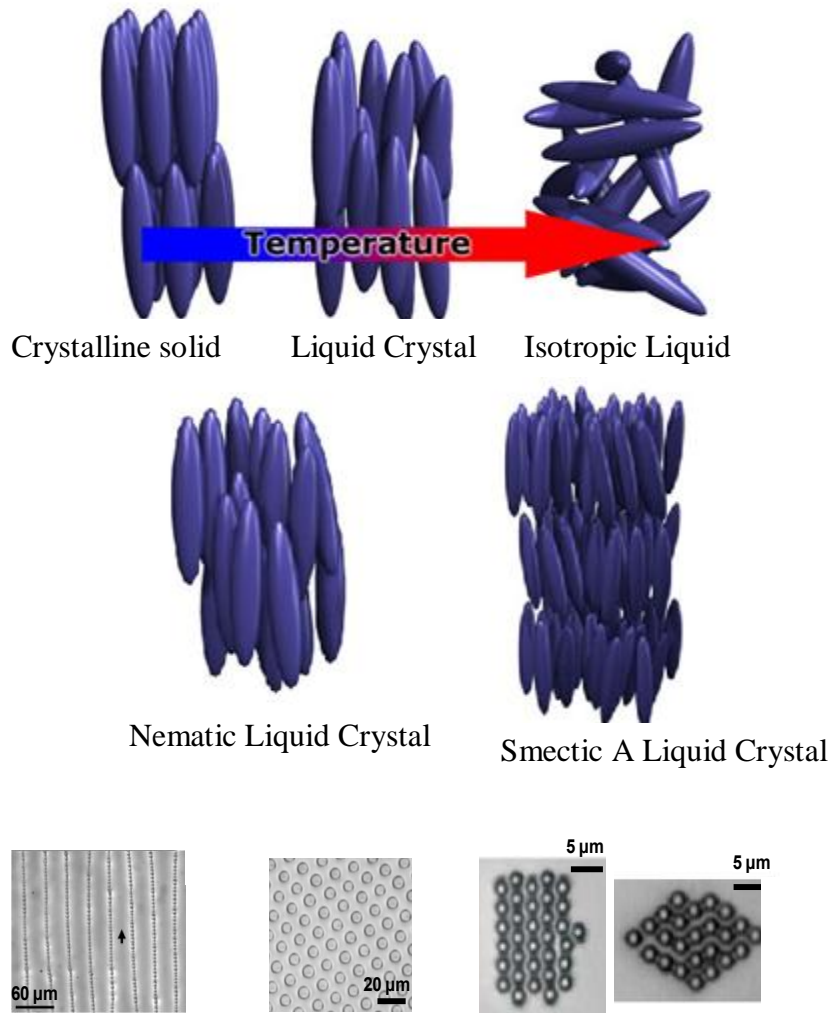


Figure 1.1: Top: schematic representations of crystal, nematic liquid crystal (NLC), smectic liquid crystal (SLC) and isotropic liquid phase [38]. Bottom: different examples of the ordered structure when μm -sized particles are immersed in NLCs [4, 12].

devices, photonics, LC displays, nanoscale electronics, electro-optical switches and the development of optical sensors. According to recent experiments [39-46] and calculations [47-50], the binding of molecules, biomolecules and viruses at solid-LC and liquid-LC functionalized interfaces distorts the local ordering of the LC and leads to inhomogeneous textures. These inhomogeneities are amplified over several length scales by LC and thus can be detected by polarized optical microscopy.

When a particle is introduced in the LC, the alignment of the LC is distorted due to the homeotropic anchoring of the LC at the surfaces of the particles. This constraint dictates conflicting orientation to the LC, which develops into topological defects. These topological defects are described by discontinuities in the director field $\mathbf{n}(\mathbf{r})$ and a significant decrease in the scalar order parameter $S(\mathbf{r})$ (i.e. LC melts at the core of the defect) [51]. These defects around particles attract each other, much like electrical charges, and the interparticle interactions are so strong that it can bind the particles into ordered structures. Generally, [Figure 1.2] there are three types of defect structures when a spherical particle is immersed in a LC: the dipole configuration (where a point defect known as hyperbolic hedgehog is formed by the nematic) [1-4, 52], the Saturn ring configuration (where a disclination loop surrounds the particle) [52-54], and the surface ring configuration (where a disclination ring sits at the surface of the particle) [1-4, 52]. Several computational and theoretical studies have focused on the topic of defect structures [52, 55-63]. The dipole configuration is observed for strong surface anchoring and micron-sized spherical particles. The Saturn ring configuration is observed upon reduction in particle size (confirmed recently through experiment) [64], magnetic and electric fields [65], and confinement conditions [54, 60, 66]. The surface ring configuration is observed upon reduction in the surface anchoring strength [52, 58]. Recently, by using a mesoscale theory where the nematic is modeled

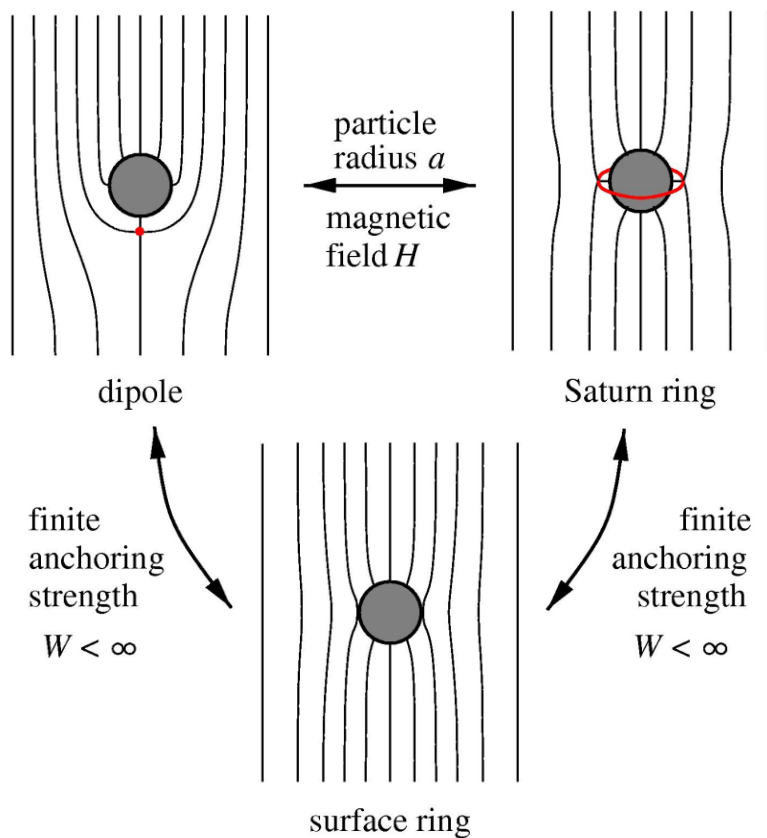


Figure 1.2: Three types of defect structures when a spherical particle is immersed in a LC: the dipole configuration, the Saturn ring configuration, and the surface ring configuration [52].

using the tensor order parameter $\mathbf{Q}(\mathbf{r})$, system of two spherical particles exhibiting dipole [67, 68] and Saturn ring [19-22] defect structures were examined. The predictions obtained by using mesoscale theory were satisfactory as compared to molecular simulation [19-22]. This comparison also proved the validity of the mesoscale theory over nm-length scales. Mesoscale theory is computationally less expensive than the molecular simulation. Thus it was used to study the behavior of several spherical nanoparticles in the bulk system [19-22] of nematic LC and inside nanochannels [24]. It was also used to study several spherocylindrical nanoparticles in nematic LC [23]. The effects of the shape and size of particles immersed in a nematic LC on the defect structures was studied recently [69]. Classical density functional theory was used to study the structure of LC around a cylindrical particle of infinite length and the interactions of such particles with structured substrates [70-72]. Force between two cylindrical particles of infinite length was also calculated by using the above theory. Dynamical simulation was performed for 2D and 3D system of disk and spherical particles immersed in LC where they were free to move due to the several body forces mediated by the LC [73-77]. Molecular dynamics simulation was also used to study the spherical nanoparticles in the nematogenic matrix of soft spherocylindrical particles [78].

In recent work, it was demonstrated that nematic braids (formed by delocalized defect lines) can stabilize colloidal clusters and 2D colloidal crystals [79]. The interaction of nanoparticles in nematic LC was studied, where a dipolar structure of 5CB was induced around the DMOAP-coated silica particles for the colloidal diameter as small as 125 nm [80]. Defect textures in the polygonal arrangement of faceted nanoparticles in nematic LC were analyzed as a function of temperature, polygon size, and polygon number [81]. Reversible association of pair of nanoparticles dispersed in nematic LC was recently found due to long-range but weak

interactions [82]. The self assembly of triangular, square and pentagonal sub-micrometer sized platelets in a thin layer of nematic liquid crystal was investigated by using 3D numerical modeling [83]. Rotational dynamics of square platelet colloids in nematic LC around multiaxis due to the application of external electric field was investigated [84].

Some experimental studies [31, 85-87] have concentrated on using LCs to manipulate nickel nanowires, carbon nanotubes and SiC nanoparticles [33-36, 85-88]. The goal of these studies was to use the rapid response of LCs to external forces (electric, magnetic, mechanical) in order to organize and realign the nanotubes/nanowires. Carbon nanotubes (CNTs) [89] have diameters on the order of nm and lengths ranging from μm to mm, and exhibit a number of desirable properties that makes them suitable for a number of applications [90, 91]. For example, CNTs have an exceptional resistance against mechanical stress and excellent thermal conductivity, making them suitable to develop composites with extraordinary mechanical and heat-dissipation properties [85, 87, 90, 91]. As a result, CNTs have attracted a lot of interest for their potential use as building blocks for nanoscale electronics and optoelectronics devices [85, 87, 90, 91]. A key issue relevant to all these potential applications is controlling the orientation of the nanotubes. Dispersion of the nanotubes in thermotropic LCs have emerged as one of the most suitable options among the different methods proposed to align CNTs [85, 90]. If the nanotubes are adequately dispersed in the LC, they will tend to align with their long axes parallel to the director field $\mathbf{n}(\mathbf{r})$ of the LC. Furthermore, and since the direction of $\mathbf{n}(\mathbf{r})$ can be easily modified by using electric and magnetic fields, flows and/or external surfaces, dispersion of CNTs in LCs provides an excellent way to manipulate and align nanotubes and semiconductor nanowires [33-36, 85-88]. After aligning the nanotubes, the LC can be polymerized into a solid to produce composite materials with unique mechanical, electronic or thermal properties. On the

other hand, most of the potential applications of CNTs in nanoscale electronics are not compatible with the presence of the LC, and therefore the LC should be separated from the nanotubes after their alignment, for example by draining it through a porous membrane [34, 35]. Furthermore, some experimental studies suggest that adding small amounts of CNTs or semiconducting nanoparticles to LCs lead to important modifications in the physical behavior of the LC, which could lead to displays and other electro-optical devices with improved properties [31, 85, 87, 92-94]. Recently, the interaction and dispersion of single walled CNTs in PEO/water solution was studied by using molecular dynamics simulations [95]. In similar work, the effect of surfactants to stabilize the dispersions of CNTs in aqueous solutions was also studied [96-98]. In other work, it was found that an efficient route toward highly ordered CNT liquid crystals is by sorting CNT via phase separation processes or dispersion processing [99].

The principles behind the use of LCs to organize particles of spherical and rod-like shapes (Figure 1.1) can be extended, in principle, to particles with shapes other than spherical, as well as particles with anisotropic surface patterns, for the assembly of ordered particle structures with unusual morphologies different from the conventional hexagonal close-packed crystals formed by spherical colloids [100-105]. A number of applications, e.g. in colloidal crystals, photonics, nanoscale electronics, memory storage and displays, are envisioned for these unusually-ordered particle arrays. For example, recently it was reported that these assemblies could be used to form metamaterials which is used for cloaking devices or light-based circuits [106]. The vast variety of particles with different shapes and surface patternings precludes the possibility of an experimental-only approach. Computer simulations will be key in this area of research to systematically explore and quickly predict the behavior of these systems, aiming at influencing future experimental efforts. In this research we carried two independent but directly

related projects:

(1) *Mesoscale simulations of faceted nanoparticles in nematic liquid crystals*. Due to the non-spherical shape of the particle, the nematic is expected to transmit torques to the particle. When a faceted particle is immersed in LC, the alignment of the LC is distorted because of the anchoring condition of the LC at the surface of the particle. Due to this distortion in the LC profile, the LC is expected to transmit torques to the particle in order to minimize its distortion around the particle. This indicates that LC distortion around the particle represents the force applied by the LC to the particle which makes it turn. If the alignment of the LC is “switched” by the external means, the particle will try to reorient back to the stable configuration. Our objective is to analyze the reorientational behavior of a faceted particle which would be relevant to the switching studies by external means. Thus, we computed torques transmitted by NLC to the faceted particle, which are presented in Chapter 2 and will be submitted soon for publication. We concentrated specifically on several faceted nanoparticles, namely cubes [107, 108] and triangular prisms [109, 110]. Our results for thermodynamic properties, such as LC defect structures and potentials of mean force for these faceted particles, have already been included in one peer-reviewed publication [111], the title page of the paper is attached in appendix A and the permission to use the paper is attached in appendix B. It was observed that several properties of the particles (e.g., shape, size) affect the strength and anisotropy of the LC-mediated interparticle interactions. The morphology and thermodynamic stability of the structures that could be assembled from these particles were predicted. Since we are interested in the interparticle interactions and arrangements, the LC does not need to be modeled at the atomic level of detail. Rather, the LC in this part of the project is modeled using a mesoscale theory in terms of the LC tensor order parameter \mathbf{Q} [51], which can allow the study of larger system sizes.

(2) *Molecular dynamics (MD) simulations of systems of CNTs and LCs.* The main goal of this part of our research is to determine how the interactions between the CNTs and LC molecules are affected by varying the molecular structure and the phase of the LC. One of the main challenges in using LCs to manipulate and align CNTs is how to efficiently disperse the nanotubes in the LC. Suspensions of CNTs in LCs are very unstable, with most of the nanotubes aggregating in a few days. The key point to obtain high-quality dispersions of CNTs in LCs is to understand the interactions between the nanotubes and the LC molecules. Molecular simulations are uniquely positioned to investigate interactions at the molecular level of detail, as well as their effects on the macroscopic properties of the systems. Such a fundamental understanding will be crucial to assist experimentalists in the development of high-quality dispersions of large concentrations of CNTs in LCs, which will be a key for using these systems in the applications like displays, nanoscale switches, nanoscale electronics, optical sensors for chemicals and biomolecules, and in the formulations of composites with unique mechanical, thermal and/or electronic properties. Chapter 3 contains our work on MD simulations of systems of CNTs and LCs, which will be submitted soon for publication. Finally, our conclusions and future directions are presented in Chapter 4.

CHAPTER 2. TORQUE TRANSMITTED BY THE NEMATIC LIQUID CRYSTAL TO THE FACETED NANOPARTICLES

2.1. Models and Methods

2.1.1. Details of the Model Systems

The system considered here is a rectangular box full of nematic LC with dimensions L_x , L_y and L_z , containing one or two particles. Figure 2.1(a) shows a schematic representation of the rectangular box filled with nematic. Periodic boundary conditions are applied to the system in x and y direction. The system is covered with walls at the top and bottom which provides homeotropic (perpendicular) anchoring to the nematic LCs. Nematic LCs also have homeotropic anchoring at the surface of the particles. This anchoring is easy to achieve experimentally by coating the surfaces with self-assembled monolayers of alkanethiols [112]. When there are no particles in the system, the nematic LC aligns its director field parallel to the z axis. The alignment of the nematic LC is distorted when a particle is introduced in the system because the orientation of the LC far away from the particle does not match with the orientation of the LC around the particle. This mismatch occurs due to the homeotropic anchoring of the LC at the surface of the particle and leads to the formation of topological defects.

In our research, we studied cube and triangular prism shaped nanoparticles with rounded edges. The cubic particle has sides with length $L = 40$ nm and rounded edges $f = 5$ nm (Figure 2.1(b)) whereas the equilateral triangular prism shaped particle has rectangular faces with length $L = 150$ nm, triangular faces with length $l = 68.7$ nm and rounded edges $f = 5$ nm (Figure 2.1(c)). We studied one- and two-particle systems in our calculations. For one cubic particle systems, the cube has its center of mass placed in the centre of the nematic cell. The cubic particle is rotated around five out of thirteen rotational symmetry axes: (1) x axis (2) $x=y=z$ axis (3) $x=0, y=z$ axis (4) $y=0, x=z$ axis and (5) $z=0, x=y$ axis (Figure 2.2(b)). Based on the octahedral symmetry of a

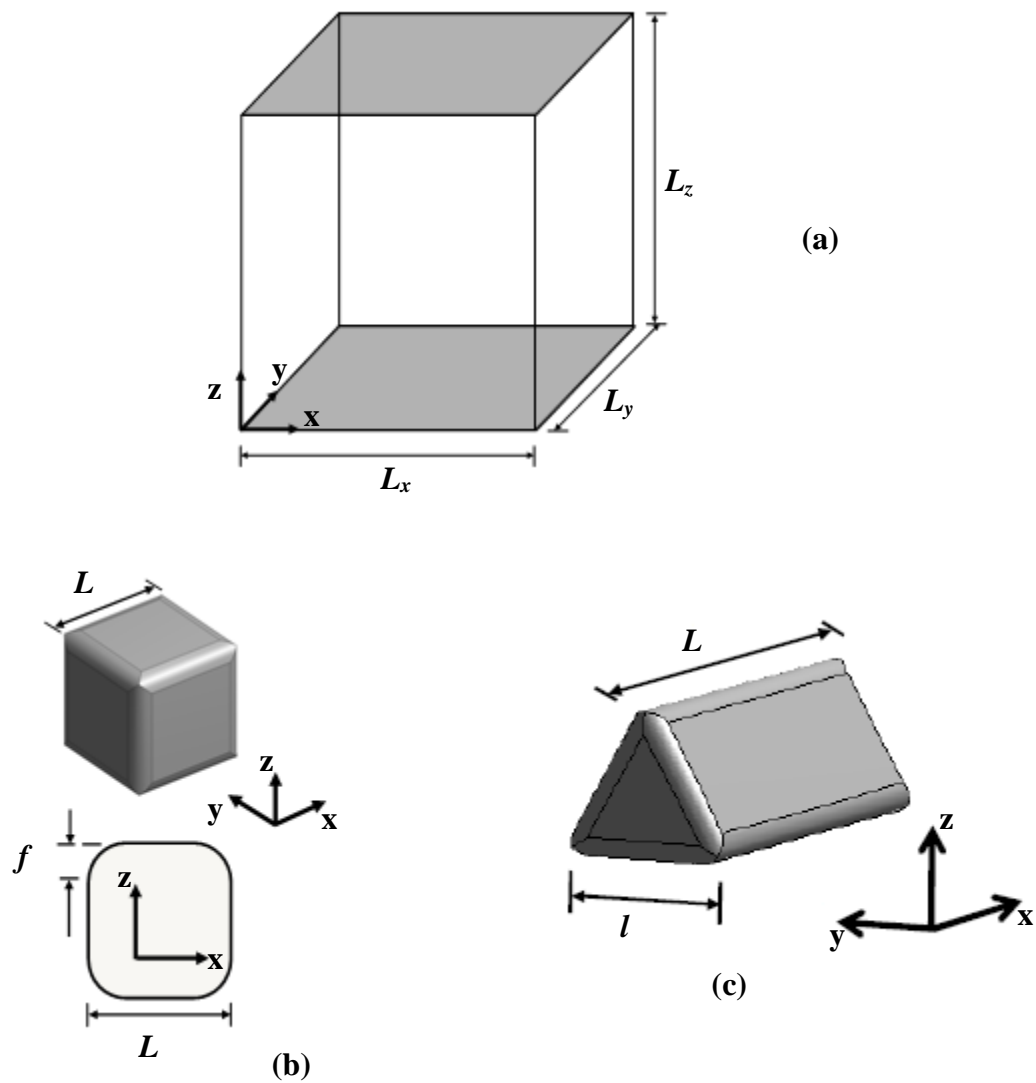


Figure 2.1: Schematic representation of (a) rectangular box full of nematic liquid crystal, (b) cubic nanoparticle, and (c) equilateral triangular prism shaped nanoparticle [111].

cube and how this symmetry is broken by the presence of a distinguished direction [i.e. the far-field director $\mathbf{n}(\mathbf{r})$, which is parallel to the z axis], rotations of the cubic particle around the other eight rotational symmetry axes will lead to configurations similar to those found for the five rotations described above. For two cubic particle systems, our research was limited to two cubic particles approaching each other, with each particle having a fixed orientation similar to the most stable configuration obtained from the one particle system. We considered two cubic particles approaching in such a way that the defects touch each other and their respective rounded edges are parallel to each other. The dimensions of the rectangular box for the one cubic particle system are $L_x = L_y = L_z = 100$ nm whereas the dimensions of the rectangular box for the two cubic particle system are $L_x = 130$ nm, $L_y = 190$ nm and $L_z = 120$ nm.

For one triangular prism system, the particle has its center of mass placed in the center of the nematic cell. The triangular prism particle is rotated around two axes (1) x axis and (2) the axis passing through two diagonal vertices of the triangular faces (Figure 2.2(a)). During these rotations, the longest side of the particle is perpendicular to the far field director. We did not rotate the triangular prism particle around the y axis because rotating the particle around the y axis will cause the longest side of the particle to become parallel to the far-field director; And when the longest side of the particle becomes parallel to the far-field director, we have large free energy penalty according to the research for the system of one spherocylindrical particle in the nematic LCs [23]. Triangular prism particle can be rotated around many axes but it was rotated around the above two axes because it will lead to configurations similar to those found for the remaining other rotations, since the far field director is parallel to z-axis. For two triangular prism particle systems, we limited our research to two particles approaching each other, with each particle having configuration similar to the stable configuration obtained from the system of

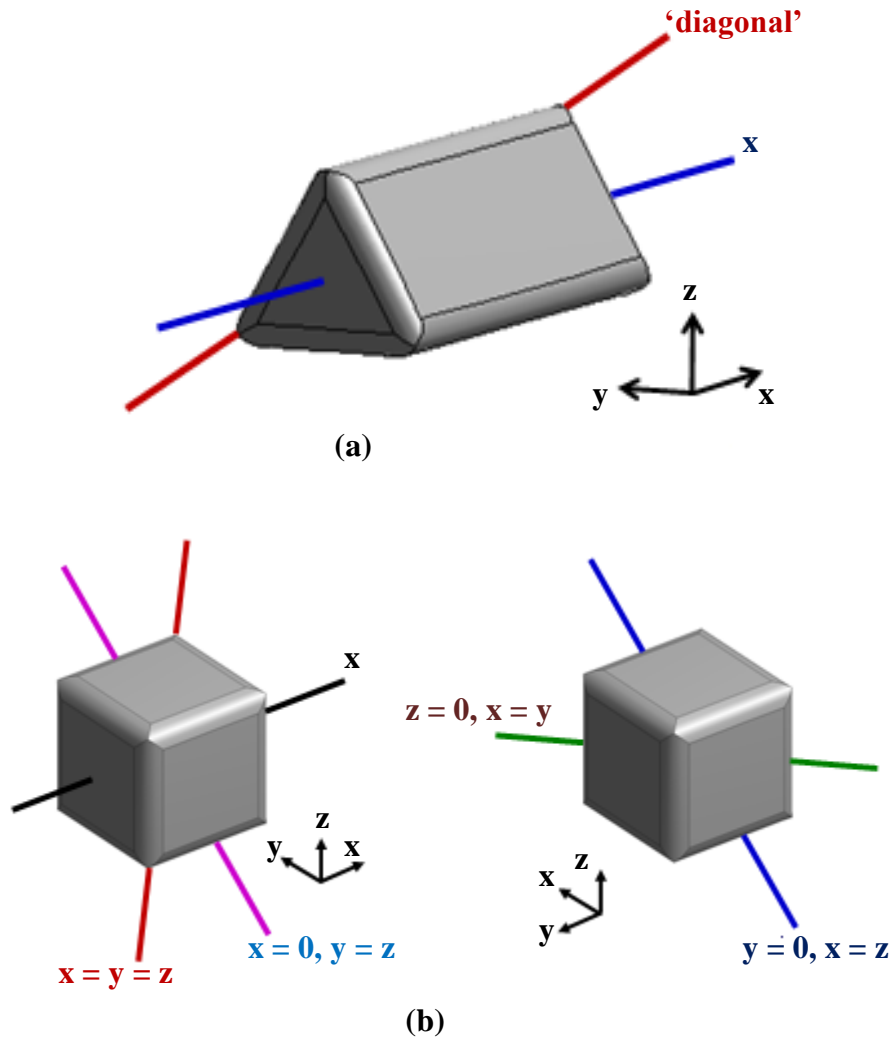


Figure 2.2: (a) The triangular prism particle is rotated around the two axes (1) only x axes (2) the axis passing through two diagonal vertices of two triangular faces as indicated in the figure. In all cases, far field director $n(r)$ is parallel to the z-axis. (b) The cubic nanoparticle is rotated around the five axes out of thirteen rotational symmetry axes as indicated in the figure [111].

one particle. Depending upon the PMF results obtained from one triangular prism particle system [111], the triangular nanoprisms can be the building blocks of several ordered arrays where the particles have their longest side rotated along x axis but their centers placed on different axes; their orientation may also vary. As a result, three ordered arrays of two nanoprisms were considered (1) centers are on the x axis and both the particles have the same orientation (linear array) (2) centers are on the y axis and both the particles have the same orientation (parallel array) and (3) centers are on the y axis, with one of the particle inverted with respect to other one (inverted parallel array). Out of three ordered arrays, according to the PMF and defect structure results [111], inverted parallel array was found to be thermodynamically more stable than the linear and parallel array. Therefore, torques for only inverted parallel array was calculated. The dimensions of the rectangular box for the one triangular prism particle system are $L_x = L_z = 1000$ nm, $L_y = 500$ nm. The dimensions of the rectangular box for the two triangular prism particle system are $L_x = 400$ nm, $L_y = 1200$ nm and $L_z = 300$ nm for inverted parallel array.

For one particle system, as a faceted particle is rotated in the nematic cell along a particular direction, there is a change in the nematic profile which applies restoring torque to the particle. In one particle system, restoring torques depends on the angle of rotation θ along a particular direction. When several particles are immersed in the LC, the reorientational behavior of a faceted particle depends on the restoring torque applied on each particle and the interaction between the particles. Therefore, torques for two particle system is calculated. For two particle system, two particles are drawn closer to one another while keeping their orientation unchanged. Since the centers of such particles appear to glide along parallel, but non-coincident planes, one would expect that the torque they exchange through the intervening liquid crystal should make

them turn. Keeping the particle's orientation unchanged amounts to apply restoring torques to both of them, which depends on the interparticle separation d .

2.1.2. Mesoscale Theory for the Nematic Liquid Crystal

The nematic LC is modeled using a mesoscale theory in terms of tensor order parameter $\mathbf{Q}(\mathbf{r})$. The tensor order parameter $\mathbf{Q}(\mathbf{r})$ is different from director field $\mathbf{n}(\mathbf{r})$ because it is free of discontinuities even at the LC defect core. The scalar order parameter $S(\mathbf{r})$ and the director field $\mathbf{n}(\mathbf{r})$ can be calculated from $\mathbf{Q}(\mathbf{r})$ by using its largest eigenvalue $2S/3$ and eigenvector [51]. In a recent study of spherical particles [19-22], the nematic LC was modeled using this mesoscale theory and the results were compared with molecular simulations where the nematic was modeled using Gay-Berne ellipsoids. It was found that the results in both the cases were in agreement down to the nm-scales, which shows the validity of the mesoscale theory at these scales. The mesoscale theory also corresponds to the particular case of Beris-Edwards formulation [113]. According to this formulation, the evolution of tensor order parameter Q as a function of position r and time t is determined by the functional derivative of free energy of the liquid crystal F with respect to tensor order parameter Q .

$$\frac{\partial \mathbf{Q}}{\partial t} = -\frac{1}{\gamma} \left[\frac{\delta F}{\delta \mathbf{Q}} - \frac{1}{3} \text{Tr} \left(\frac{\delta F}{\delta \mathbf{Q}} \right) \mathbf{I} \right] \quad (1)$$

γ is the kinetic coefficient associated with the rotational viscosity of the liquid crystal and it is assumed constant. The functional derivative of the free energy of the liquid crystal F with respect to tensor order parameter Q is assumed to be symmetrized in Equation (1). The following equation represents the free energy of the nematic liquid crystal and it is divided into three parts.

$$F = \int d\mathbf{r} f_{LdG}(\mathbf{r}) + \int d\mathbf{r} f_e(\mathbf{r}) + \int dS f_s(\mathbf{r}) \quad (2)$$

The first term is Landau-de Gennes [51] expansion representing the short range interactions that drive the bulk isotropic to nematic phase transition.

$$f_{LdG} = \frac{A}{2} \left(1 - \frac{U}{3} \right) \text{Tr}(\mathbf{Q}^2) - \frac{AU}{3} \text{Tr}(\mathbf{Q}^3) + \frac{AU}{4} [\text{Tr}(\mathbf{Q}^2)]^2 \quad (3)$$

A and U are the constants in the above equation which depends on the liquid crystal. A represents the energy scale of the model and U governs the bulk scalar order parameter

$$S_{bulk} = \frac{1}{4} \left(1 + 3 \sqrt{1 - \frac{8}{3U}} \right) \quad (4)$$

When $0 < U < 2.7$, the system is isotropic but at $U > 2.7$, the system is nematic. $U = 3$ and $8/3$ are the metastability limit for isotropic and nematic phase respectively. The third term in Equation (2) represents the contribution of surface to the free energy of the liquid crystal and accounts for anchoring of the liquid crystal at the surface of the particle. We are concerned with the limit of the infinitely strong homeotropic anchoring of the liquid crystal at the surface of the particle. The prescribed homeotropic anchoring of the liquid crystal at the surface should be satisfied at the limiting case otherwise the term f_s diverges. The homeotropic anchoring of the liquid crystal is applied at the surface through boundary conditions for calculation purposes.

The second term in Equation (2) is the contribution of the long range elastic forces of the liquid crystal to the free energy and introduces a free energy penalty related to the gradients of the tensor order parameter field. In our research, we used one elastic constant approximation [51] where the constants K_{11} (splay), K_{22} (twist) and K_{33} (bend) have common value. During a recent study of spherocylindrical particles in a nematic liquid crystal [23], it was found that the results obtained from the one elastic constant approximation were similar to those from the three elastic constant approximation [113-115]. The term f_e in the Equation (2) is as follows:

$$f_e = \frac{L_1}{2} \frac{\partial Q_{ij}}{\partial x_k} \frac{\partial Q_{ij}}{\partial x_k} \quad (5)$$

In the above equation, $i, j, k \in x, y, z$, the Einstein summation convention over the repeated indices is used. When the Equation (1) is evaluated using Equation (2), (3) and (5), we obtain the set of partial differential equations of Q as follows:

$$\frac{\partial Q_{ij}}{\partial t} = -\frac{1}{\gamma} \left\{ A \left(1 - \frac{U}{3} \right) Q_{ij} - AU \left[Q_{ik} Q_{kj} - \frac{\delta_{ij}}{3} Q_{kl} Q_{kl} - Q_{ij} (Q_{kl} Q_{kl}) \right] - L_1 \frac{\partial}{\partial x_k} \left(\frac{\partial Q_{ij}}{\partial x_k} \right) \right\} \quad (6)$$

The above equation gives the set of partial differential equations of Q which is solved numerically for all the systems in our study. The dimensionless constants are $A = 1$, $U = 6$, $\gamma = 400$ and $L_1 = 1$, corresponding to $S(\text{bulk}) = 0.81$. These parameters correspond to the elastic constant $K = 5$ pN (one elastic constant approximation) and viscosity = 0.04 Pa.s using the scaling factors for pressure (10^5 Pa), length (10 nm) and time (1 ns). These values of constants represent a low molecular weight liquid crystal like 5CB. For dimensional analysis, we can obtain a characteristics length scale (ξ) for the spatial variation of Q [116]. The characteristics length scale (ξ) is equal to 17.3 for calculation purpose and its equation is presented as follows:

$$\xi = \sqrt{18L_1/AU} \quad (7)$$

Since Q is traceless, it has five independent components of tensor order parameter Q (Q_{xx} , Q_{yy} , Q_{xy} , Q_{xz} and Q_{yz}). In order to obtain these components, Equation (6) was solved by using finite elements and the COMSOL multiphysics package [117]. We used the time – dependent algorithm DASPK, combined with the linear system solver GMRES and the incomplete LU preconditioner [117] to solve all the equations. In order to minimize the free energy, the Equation (6) is solved for sufficiently long period of time until the solution has almost no numerical variation. According to our previous studies [23, 24, 69], we carried out the simulation

using unstructured meshes containing tetrahedral, linear Lagrange elements set as default mesh by COMSOL Multiphysics [118]. Several grid densities were used and it was observed that we require about 51,865 finite elements in order to make numerical solution mesh independent. Mesh was finer near the wall and the nanoparticle, where the variation of Q is strong and curvature effects are present. For cubic particles, the minimum length of the finite elements in our finest grid size is $\sim 1.1 \times 10^{-4}L$ which is comparable to those reported by Fukuda et al [59]. The initial conditions of Q for the simulation are scalar order parameter $S(r)$ equal to $S(\text{bulk})$ and the director field aligned along the z direction. It was found that the results are similar when the calculations are started from the LC in an isotropic phase. The scalar order parameter at the surface of the particle was also set to $S(\text{bulk}) = 0.81$. We can visualize the nematic LC defect structure by using different methods [119-122]. According to previous studies [19-24, 69], we use the contour $S = 0.30$ to visualize the defect because $S = 0.30$ is the lowest possible value of the scalar order parameter for the stable nematic LC in our model [113, 116]. The free energy is calculated by integrating the Equations 2, 3 and 5 over the volume of the system. The torque T is calculated by the following equation [123]

$$T = \oint \mathbf{L} v dS \quad (8)$$

where v is the vector of normals acting on the surface of the particles and L is the couple stress tensor. The equation for L is given as follows

$$\mathbf{L}_{ij} = 2\varepsilon_{ikl} Q_{km} \frac{\partial f}{\partial (\partial Q_{ml} / \partial x_j)} \quad (9)$$

where ε is the Ricci's alternator and f is the free energy of the system, which includes Landau de Gennes expansion and long range elastic forces of liquid crystal (Equation (2)). The three components of torque are calculated by numerical integration of the Equation (8) and (9) over the surface of the particles.

2.2. Results and Discussions

2.2.1. Triangular Prism Shaped Particle

2.2.1.1. Triangular Prism Shaped Particle Rotated Around x axis

The PMF value of one equilateral triangular prism shaped nanoparticle rotated around x-axis is presented in paper [111]. PMF value represents the stability of a particular orientation. If the PMF value is high, then the alignment of the NLC around the particle is highly distorted and vice versa. Thus, at $\theta = 30^\circ$, the NLC is the most distorted around the triangular prism shaped particle because of the highest PMF value and at $\theta = 0^\circ$ and 60° , the NLC is the least distorted because of the lowest PMF value [111]. The maxima and minima in the PMF profile represent the symmetric orientation of the particle. Thus, at $\theta = 0^\circ, 30^\circ$ and 60° , the orientation of the triangular prism shaped particle is symmetric [111]. Figure 2.3 shows the total torque transmitted by NLC on one triangular prism shaped nanoparticle, rotated around the x axis, as a function of angle of rotation. Total torque is calculated as the dot product of the unit vector along the axis of rotation and the individual components of torques in x, y and z direction. Figure 2.4 shows the 3D visualizations of the NLC distortion around one triangular prism shaped particle. Figure 2.5 shows the contour map of balanced NLC distortion around the symmetric orientation of the particle.

Torque profile for one faceted nanoparticle in the NLC is mostly divided into in-plane and out-of-plane torques [83]. In-plane torque is observed when the NLC distortion around the particle is completely converted into torque, whereas, out-of-plane is observed when only a part of distortion is converted into torque. When a triangular prism shaped particle is rotated around the x-axis, the in-plane torque develops as the angle of rotation increases from the stable configuration ($\theta \sim 0^\circ$) to $\theta \sim 20^\circ$ (Figure 2.3), because the orientation of the particle becomes

asymmetric (Figure 2.4). As the orientation becomes asymmetric, the NLC distortion becomes unbalanced around the particle (Figure 2.5) and thus, the distortion gets completely converted into torque. Hence, from $\theta \sim 0^\circ$ to 20° , the torque transmitted by the NLC to the particle increases (Figure 2.3), as the NLC distortion around the particle increases (Figure 2.4). Out-of-plane torque develops as the angle of rotation increases from $\theta \sim 20^\circ$ to $\theta \sim 30^\circ$ (Figure 2.3), because the orientation of the particle becomes symmetric (Figure 2.4). As the orientation becomes symmetric, the NLC distortion becomes balanced around the particle and thus, only a part of distortion gets converted into torque (Figure 2.5). Hence, for $\theta \sim 20^\circ$ to 30° , the torque transmitted by the NLC to the particle decreases (Figure 2.3), as the NLC distortion around the particle increases (Figure 2.4). The magnitude of the out-of-plane torque is similar to that of in-plane torque but varies more with respect to the angle of rotation, which is evident by its large slope (Figure 2.3). According to our previous work [111], isolated triangular nanoprism prefers to orient with one of its rectangular sides perpendicular to the far field director $\mathbf{n}(\mathbf{r})$ because NLC distortion around the preferred orientation is the smallest. Therefore, stable configuration occurs at fixed interval with $\theta \sim 0^\circ$ and 60° (Figure 2.4). These stable configurations have zero torque in the torque profile (Figure 2.3). When the particle orients with one of its rectangular sides parallel to the far field director $\mathbf{n}(\mathbf{r})$ (i.e. out-of-plane orientations), the torque reaches maximum (see the enclosed blue rectangular region in Figure 2.3 and the corresponding 3D visualization in Figure 2.4) because NLC around the particle is highly distorted (Figure 2.4). These out-of-plane orientations are unstable configurations and when a particle is oriented at these configurations, it immediately moves away from that state, which is evident by the large slope within the enclosed blue rectangular region in Figure 2.3, and then it slowly reorients itself to the closest stable configuration.

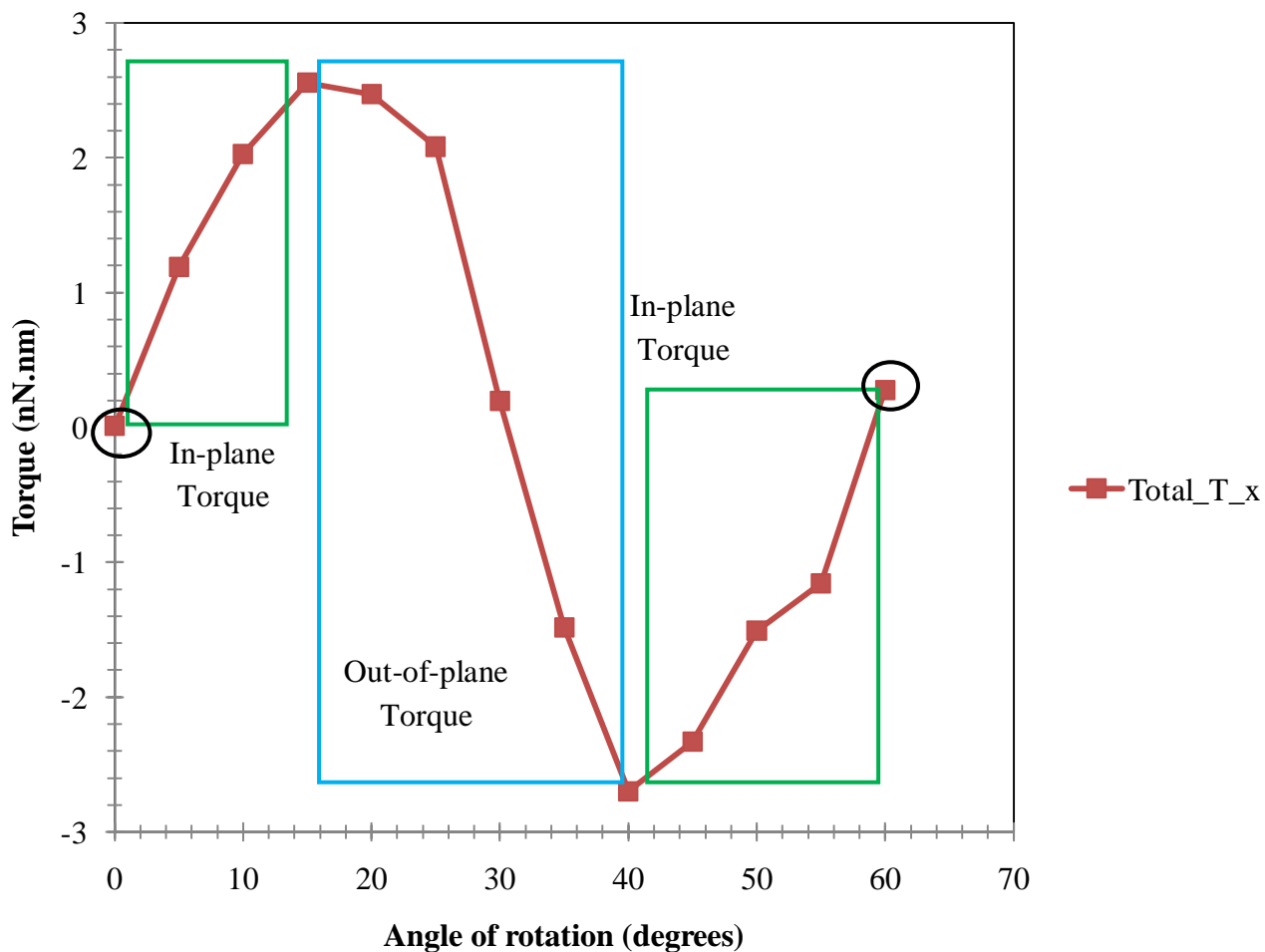


Figure 2.3: Total torque transmitted by the nematic liquid crystal on the one equilateral triangular prism shaped nanoparticle, rotated around the x axis, as a function of angle of rotation. The enclosed blue rectangular region represents angles with out-of-plane rotation and the enclosed green region represents angles with in-plane rotation. Circles indicate the stable and zero torque configuration.

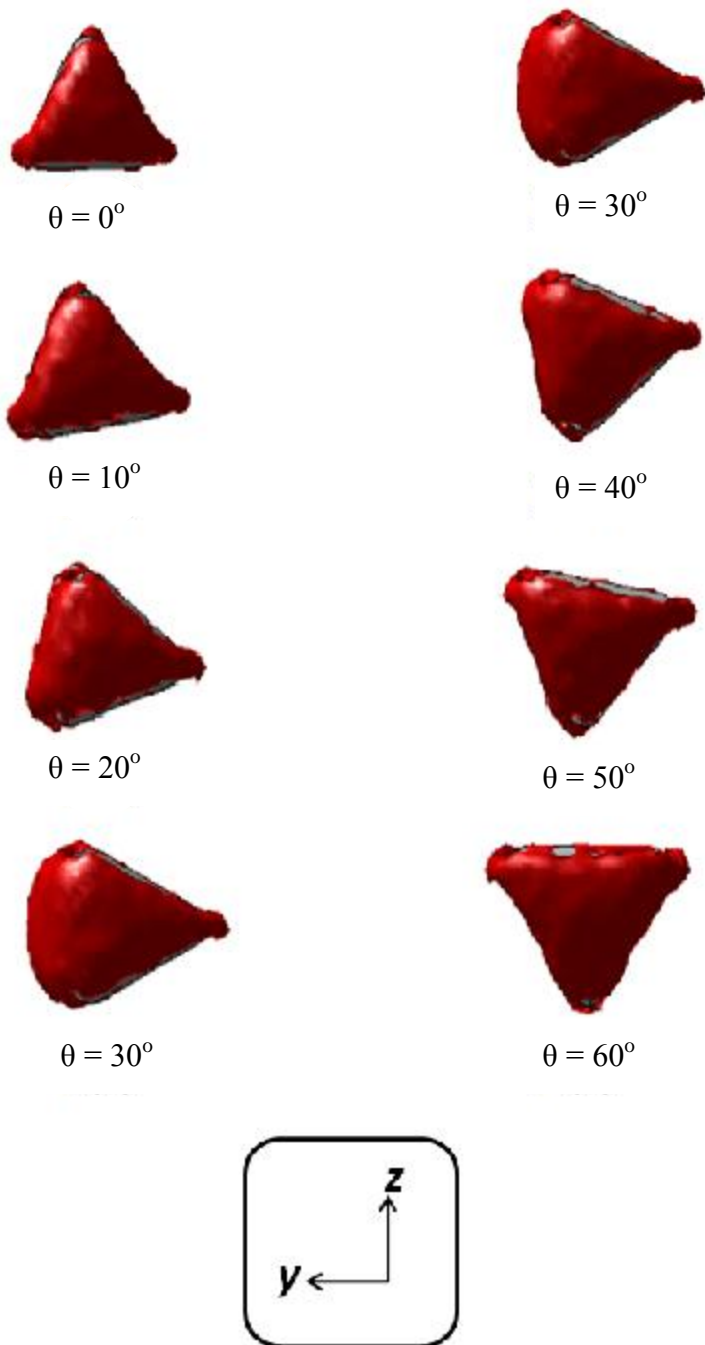


Figure 2.4: 3D visualizations of the NLC distortion around the equilateral triangular prism shaped particle when the particle is rotated around x axis at angle θ .

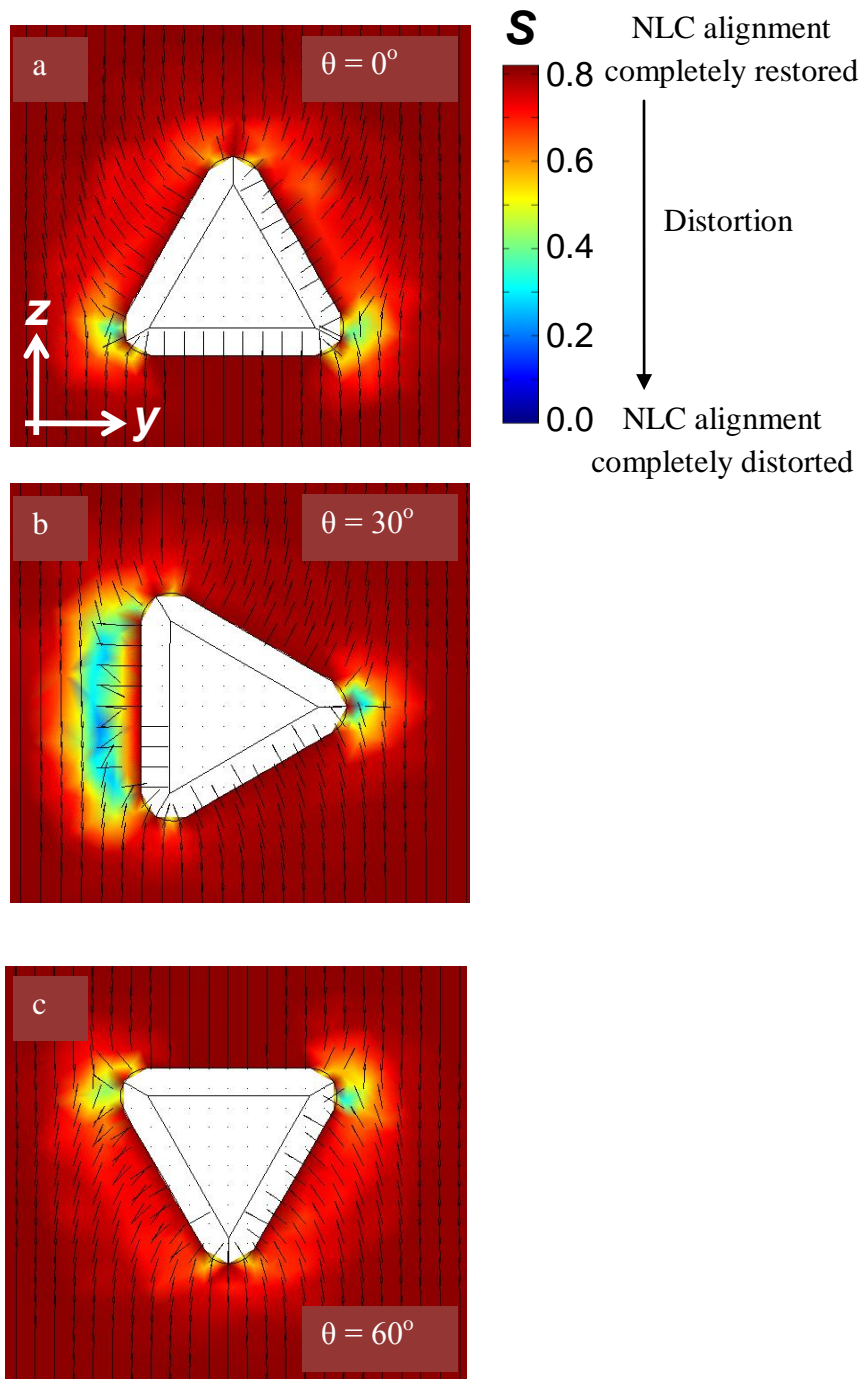


Figure 2.5: Contour map of the NLC distortion (scalar order parameter S) around the equilateral triangular prism shaped particle rotated around x axis at angle (a) $\theta = 0^\circ$ (b) $\theta = 30^\circ$ and (c) $\theta = 60^\circ$. The orientations a, b and c are symmetric, and the NLC distortion around those orientations is balanced because the scalar order parameter S near one of the three sides is similar to that of the other side. If the NLC distortion is unbalanced around the particle, the S would be different on all the three sides.

2.2.1.2. Two Triangular Prism Shaped Particle System

Figure 2.6 shows x, y, and z components of torque transmitted by the NLC to the triangular prism nanoparticles approaching each other along the z-y plane. Our results indicate that x component of the torque transmitted by the NLC to the triangular prism particles ($T_{x(1,2)}$) is more significant than the y ($T_{y(1,2)}$) and z ($T_{z(1,2)}$) component of the torque for all the interparticle distances considered. The variation in the magnitude of $T_{x(1,2)}$ is observed for $d < 40$ nm whereas the variation in the magnitude of $T_{y(1,2)}$ and $T_{z(1,2)}$ is observed when the two nanoparticles are very close to each other ($d \sim 0$ nm) (Figure 2.6). The torque $T_{x(1,2)} \sim 0$ when the triangular prism particles are separated by a interparticle distance $d > 40$ nm. However, as d is reduced, $T_{x(1,2)}$ increases, reaching a maximum value of ~ 3 nN.nm at $d \sim 10$ nm. This positive torque in the x direction will rotate the triangular prism particles around their long axis in an anticlockwise direction. According to our previous work [111], stable triangular nanoprisms prefer to be close to each other ($d \sim 5$ nm) because the surface area of the NLC distortion around the particles is the smallest. Since the particles approach each other along the z-y plane and one of the particles is inverted with respect to the other one, as the interparticle distance decreases from $d \sim 10$ nm to 0 nm, the repulsion between the particles produces the significant change in all the three components (x, y and z) of torque. Hence, $T_{z(1,2)}$ and $T_{y(1,2)}$ show opposite torques with values ~ 2.2 nN.nm and ~ 1 nN.nm respectively, whereas $T_{x(1,2)}$ shows positive torques with similar magnitude of ~ 2.5 nN.nm (Figure 2.6). This behavior is observed because combining both the particles in a inverted parallel array leads to a parallelogram like structure (Figure 2.7). Since this structure behaves as a single particle and has its center on the y axis, it develops $T_{x(1,2)}$ with similar magnitude and direction. The magnitude of the torques transmitted by the NLC to the triangular prism particles can be reduced to some extent by making the particles follow a

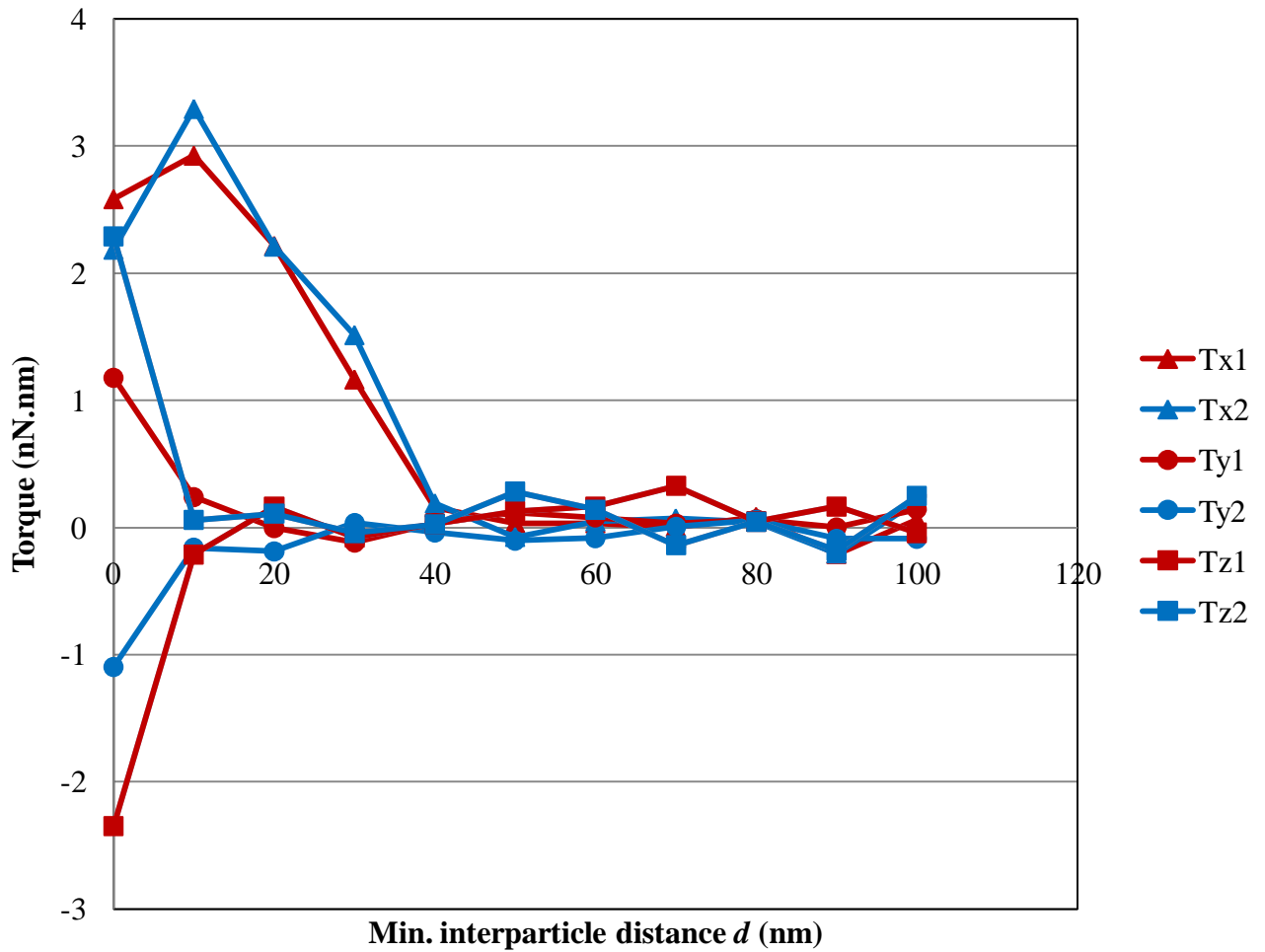


Figure 2.6: Torque transmitted by the nematic liquid crystal on the two equilateral triangular prism shaped particle system as a function of minimum surface-to-surface interparticle distance d . Triangles: x component of torque acting over particle 1 (red) and 2 (blue). Circles: y component of torque acting over particle 1 (red) and 2 (blue). Squares: z component of torque acting over particle 1 (red) and 2 (blue).

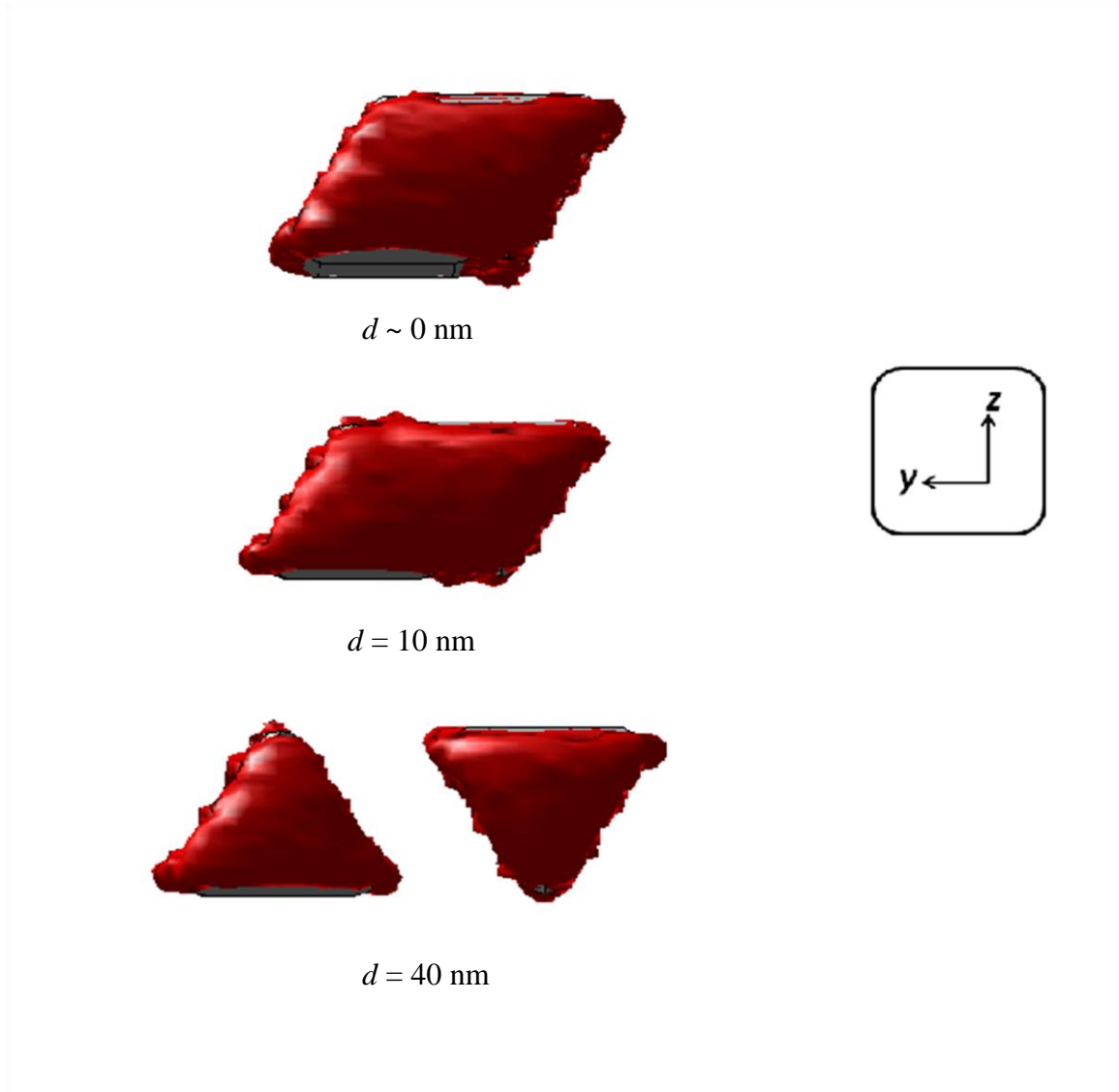


Figure 2.7: 3D visualizations of the NLC distortion around the two equilateral triangular prism shaped particles separated by the interparticle distance d .

“diagonal” trajectory while approaching each other. Recently, Hung [69] observed that the magnitude of the torque $T_{x(1,2)}$ transmitted by the NLC to the long spherocylindrical particles decreased by 45%, when the particles approached each other via “diagonal” trajectory.

2.2.2. Cubic Particle

The PMF value of one cubic nanoparticle rotated around the five symmetry axes is presented in paper [111]. As explained in section 2.2.1, PMF value represents the stability of the particular orientation. The total torque transmitted by NLC on a cubic nanoparticle rotated around the $y=0, x=z$ axis is similar to that rotated around the $x=0, y=z$ axis. Therefore, the results for the torque transmitted by the NLC on a cubic nanoparticle rotated around the $y=0, x=z$ axis are not presented. Figure 2.8, 2.10, 2.12 and 2.14 shows total torque transmitted by NLC on a cubic nanoparticle rotated around the $x=y=z$ axis, $x=0, y=z$ axis, $z=0, x=y$ axis and x axis respectively. In case of a cubic particle rotated around the x axis, $x=y=z$ axis and $z=0, x=y$ axis, total torque is calculated as the dot product of the unit vector along the axis of rotation and the individual components of torques in x, y and z direction, whereas, in case of a cubic particle rotated around $x=0, y=z$ axis, total torque is calculated as the dot product of the unit vector along the axis of rotation and the absolute value of the individual components of torques in x, y and z directions.

When a particle is rotated around $x=0, y=z$ axis and $z=0, x=y$ axis, two, out of the three, individual components of torques are significant in defining the total torque around the axis of rotation. However, in case of a particle rotated around $x=0, y=z$ axis, the two significant individual components of torque have opposite signs, therefore the total torque around the axis of rotation would be invalid. Hence, the absolute value of the significant individual components is computed. Figure 2.9, 2.11, 2.13 and 2.15 shows the 3D visualizations of the NLC distortion

around the cubic particle when the particle is rotated at angle θ around the four symmetry axes mentioned above.

2.2.2.1. Cubic Particle Rotated Around $x=y=z$ axis and $x=0, y=z$ axis

When a cubic particle is rotated around the $x=y=z$ axis and $x=0, y=z$ axis, the in-plane torque develops as the angle of rotation decreases from the zero torque configuration ($T = 0$) to $\theta \sim 30^\circ$ (Figure 2.8 and 2.10), because the orientation of the particle becomes asymmetric [111]. As the orientation becomes asymmetric, the NLC distortion becomes unbalanced around the particle and thus, distortion gets completely converted into torque. Hence, from $T=0$ configuration to $\theta \sim 30^\circ$, the torque transmitted by the NLC to the particle increases (Figure 2.8 and 2.10), as the NLC distortion around the particle increases (Figure 2.9 and refer [111]). Out-of-plane torque develops as the angle of rotation decreases from $\theta \sim 30^\circ$ to $\theta \sim 0^\circ$ (Figure 2.8 and 2.10), because the orientation of the particle becomes symmetric [111]. As the orientation becomes symmetric, the NLC distortion becomes balanced around the particle and thus, only a part of distortion gets converted into torque. Hence, from $\theta \sim 30^\circ$ to 0° , the torque transmitted by the NLC to the particle decreases (Figure 2.8 and 2.10), as the NLC distortion around the particle increases (Figure 2.9 and refer [111]).

According to our previous work [111], isolated nanocube prefers to orient with none of its sides perpendicular to the far field director $\mathbf{n}(\mathbf{r})$ because the NLC distortion around the preferred orientation is the smallest. Therefore, particle has the most stable configurations at fixed interval with $\theta = 60^\circ$ for $x=y=z$ axis and $\theta = 90^\circ$ for $x=0, y=z$ axis (Figure 2.8 and 2.10). In order to have a zero torque, a configuration should have high degree of symmetry along with low NLC distortion around it. Thus, in case of $x=y=z$ axis and $x=0, y=z$ axis, the most stable configuration is also a zero torque configuration because of its high degree of symmetry (refer

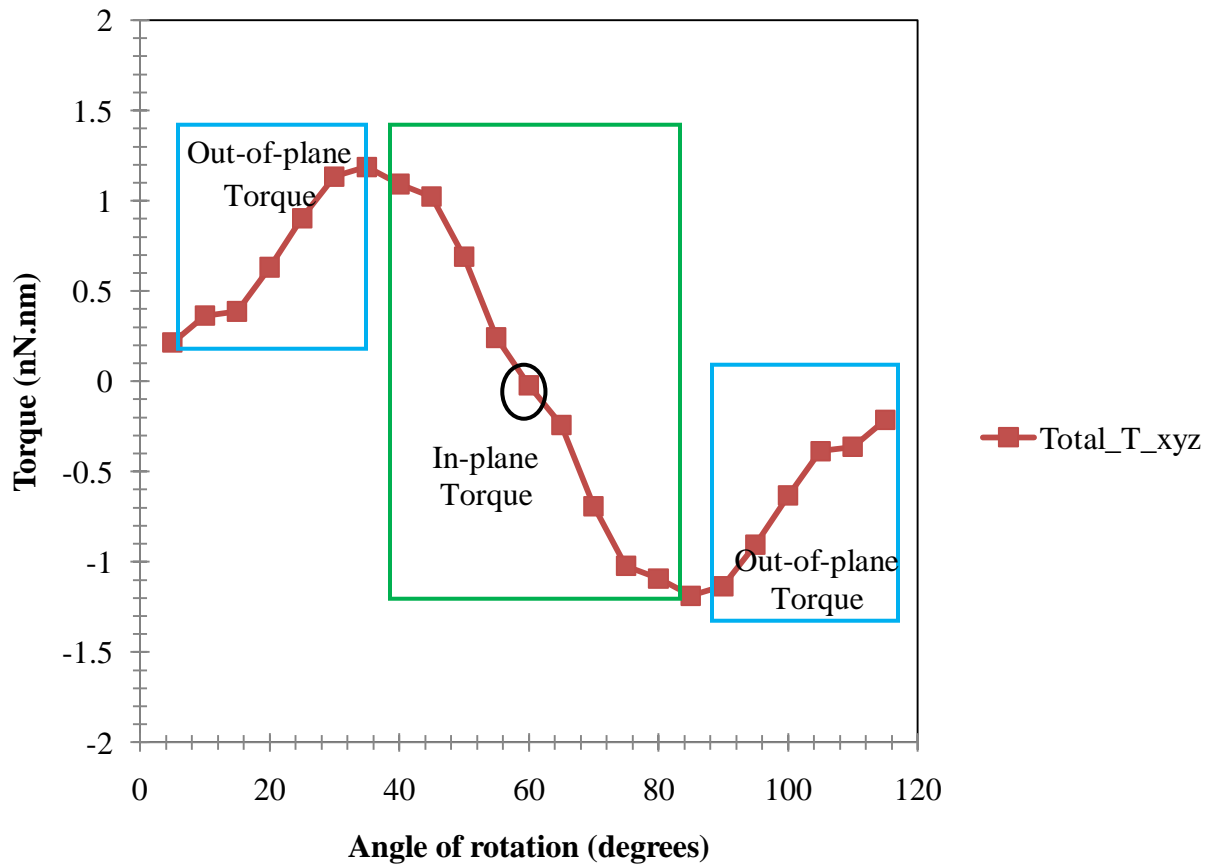


Figure 2.8: Total torque transmitted by the nematic liquid crystal on the one cubic nanoparticle, rotated around the $x=y=z$ axis, as a function of angle of rotation. The enclosed blue rectangular region represents angles with out-of-plane rotation and the enclosed green region represents angles with in-plane rotation. Circle indicates the most stable and a zero torque configuration.

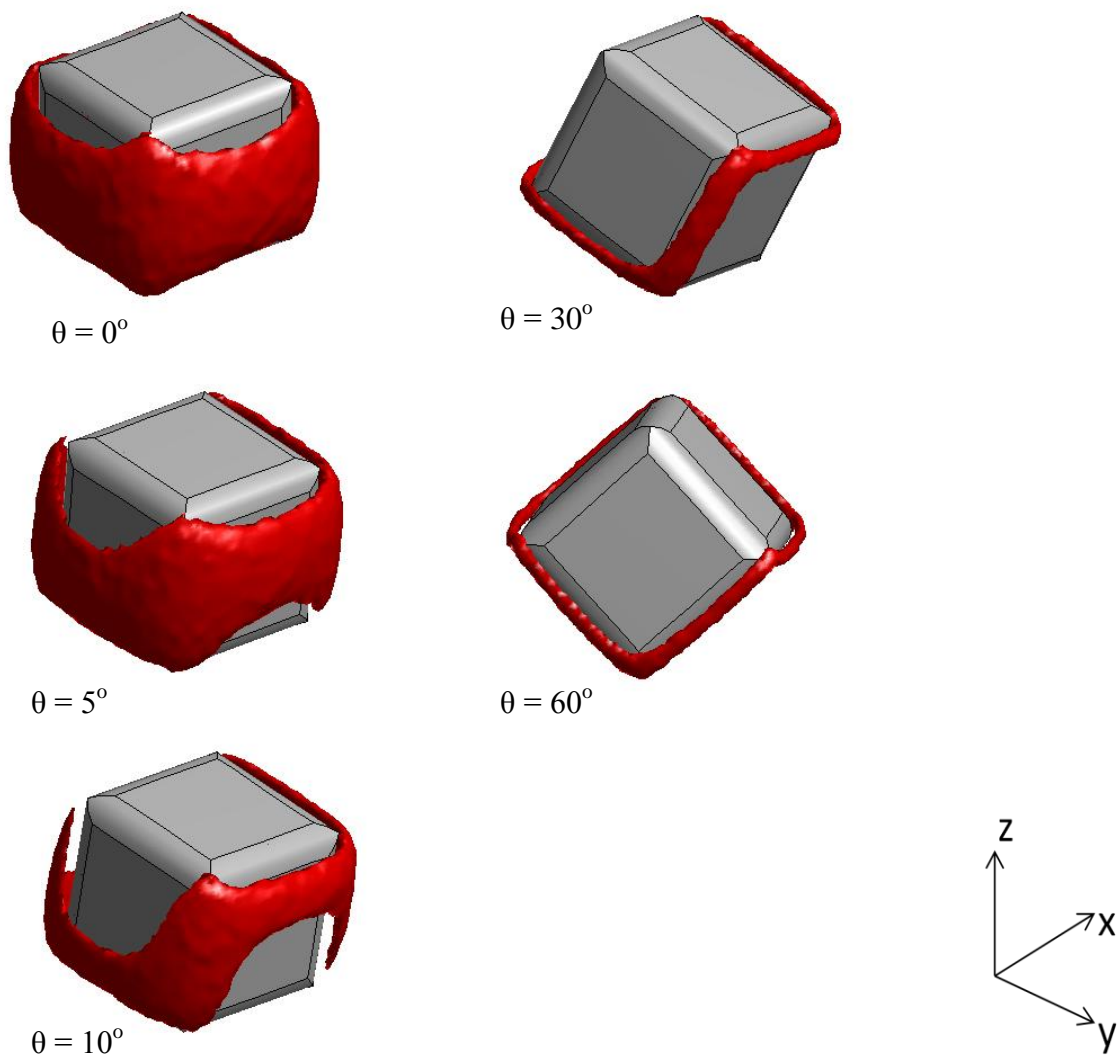


Figure 2.9: 3D visualizations of the NLC distortion around the cubic particle when the particle is rotated around $x=y=z$ axis at angle θ .

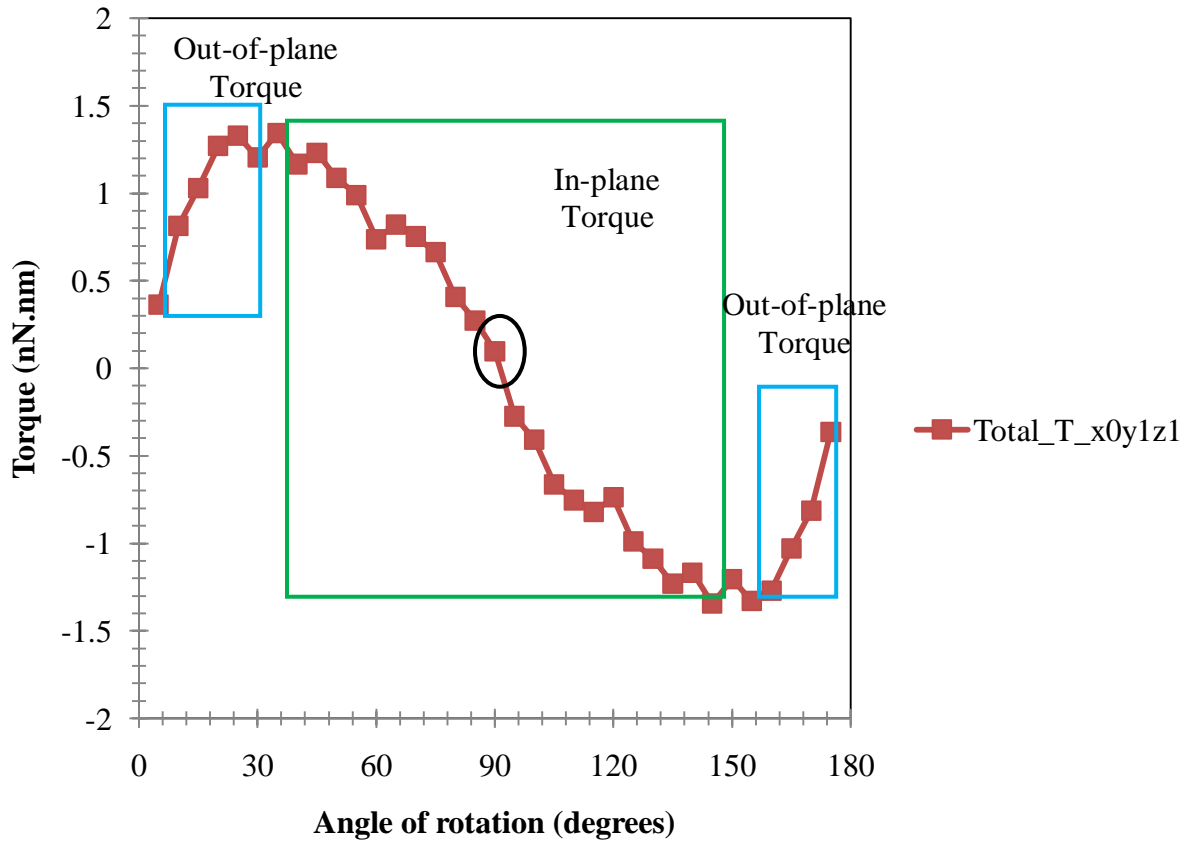


Figure 2.10: Total torque transmitted by the nematic liquid crystal on the one cubic nanoparticle, rotated around the $x=0, y=z$ axis, as a function of angle of rotation. The enclosed blue rectangular region represents angles with out-of-plane rotation and the enclosed green region represents angles with in-plane rotation. Circle indicates the most stable and a zero torque configuration.

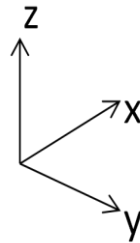
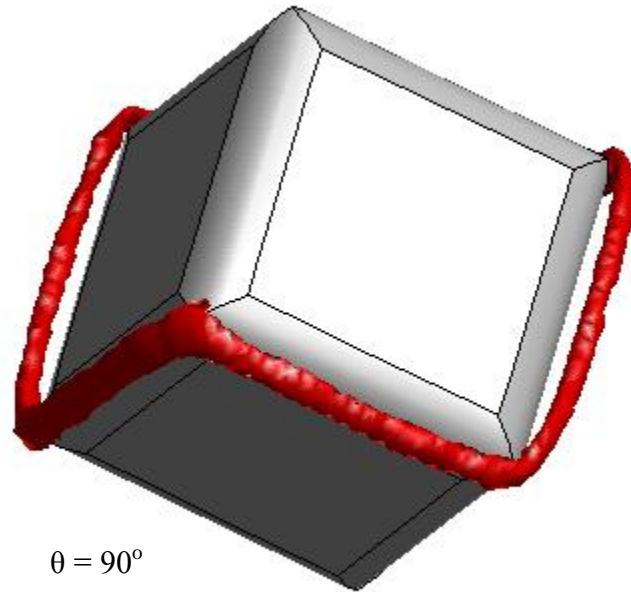


Figure 2.11: 3D visualizations of the NLC distortion around the cubic particle when the particle is rotated around $x=0, y=z$ axis at angle $\theta = 90^\circ$.

[111] and the corresponding 3D visualization in Figure 2.9 and 2.11). When a cubic particle orients with its four lateral faces parallel to the far field director $\mathbf{n}(\mathbf{r})$ (i.e. out-of-plane orientations), the torque reaches maximum (see the enclosed blue rectangular region in Figure 2.8 and 2.10, and the corresponding 3D visualization in Figure 2.9) because NLC around the particle is highly distorted. The magnitude of the in-plane torque is similar to that of out-of-plane torque (Figure 2.8 and 2.10). When a cubic particle is oriented around $x=0, y=z$ axis, out-of-plane torque varies more with the angle of rotation, as compared to that of in-plane torque, due to the larger slope (Figure 2.10). Therefore, when a cubic particle is oriented at unstable configuration (out-of-plane orientations), along the $x=0, y=z$ axis, it moves away immediately from that state and then slowly reorients itself to the stable configuration (in-plane orientations). In case of a cubic particle oriented around the $x=y=z$ axis, in-plane and out-of-plane torques varies similar with respect to the angle of rotation, due to the same slope. Hence, for a cubic particle oriented at unstable configuration along the $x=y=z$ axis, the movement of the particle from that state and then the reorientation to the stable configuration has the similar speed (Figure 2.8).

2.2.2.2 Cubic Particle Rotated Around $z=0, x=y$ axis

A cubic particle oriented along $z=0, x=y$ axis has a stable configuration at $\theta \sim 55^\circ$ and a zero torque configuration at $\theta = 90^\circ$. The stable configuration along $z=0, x=y$ axis does not have a zero torque because of its asymmetry. Hence, when a cubic particle is rotated around the $z=0, x=y$ axis, only out-of-plane torque develops as the angle of rotation either increases or decreases from the stable configuration $\theta \sim 55^\circ$ (Figure 2.12), because the orientation of the particle becomes symmetric on either side [111]. However, as the angle of rotation decreases from $\theta \sim 20^\circ$ to 0° , we observe an unconventional torque because of the rapid decrease in the NLC

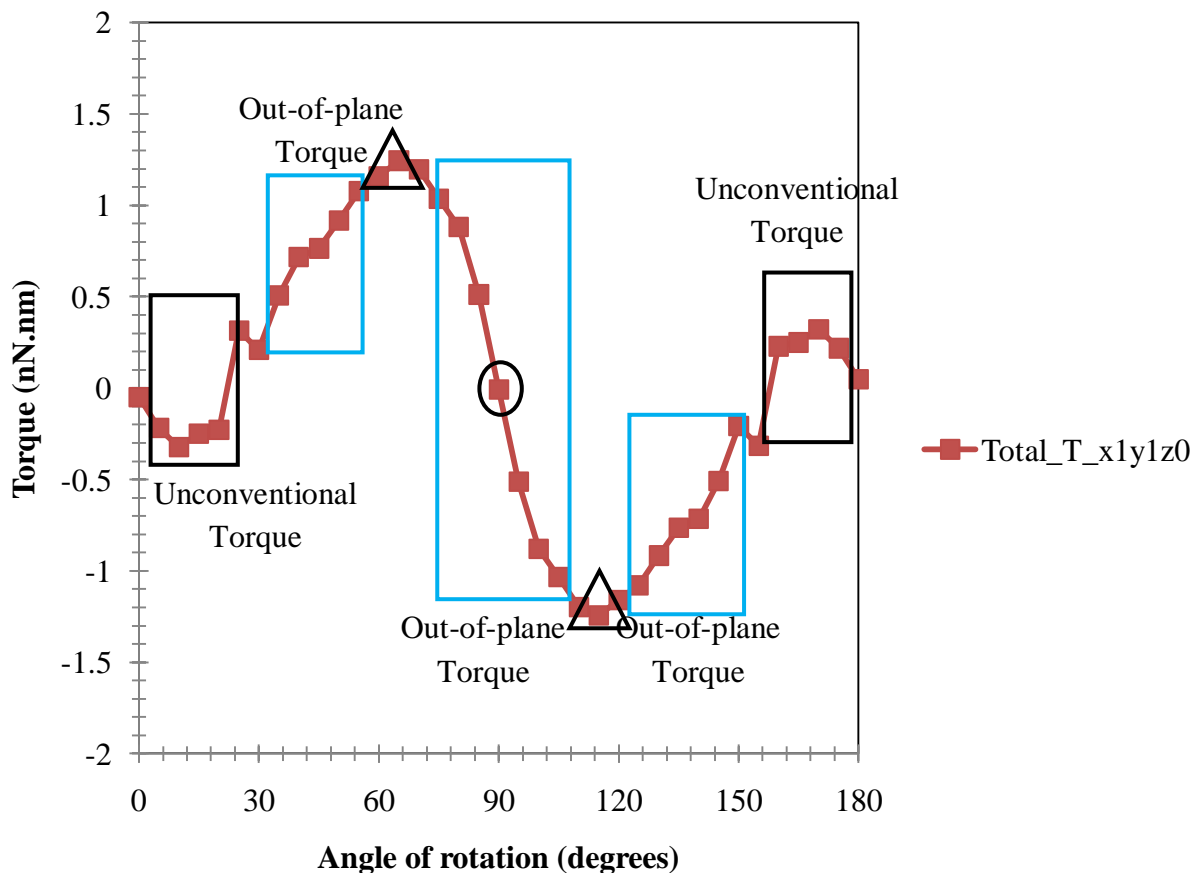


Figure 2.12: Total torque transmitted by the nematic liquid crystal on the one cubic nanoparticle, rotated around the $z=0$, $x=y$ axis, as a function of angle of rotation. The enclosed light blue rectangular region represents angles with out-of-plane rotation 1, the enclosed dark blue region represents angles with out-of-plane rotation 2 and the enclosed black region represents angles with unconventional rotation. The circle indicates the zero torque configuration and the triangle indicates the most stable configuration.

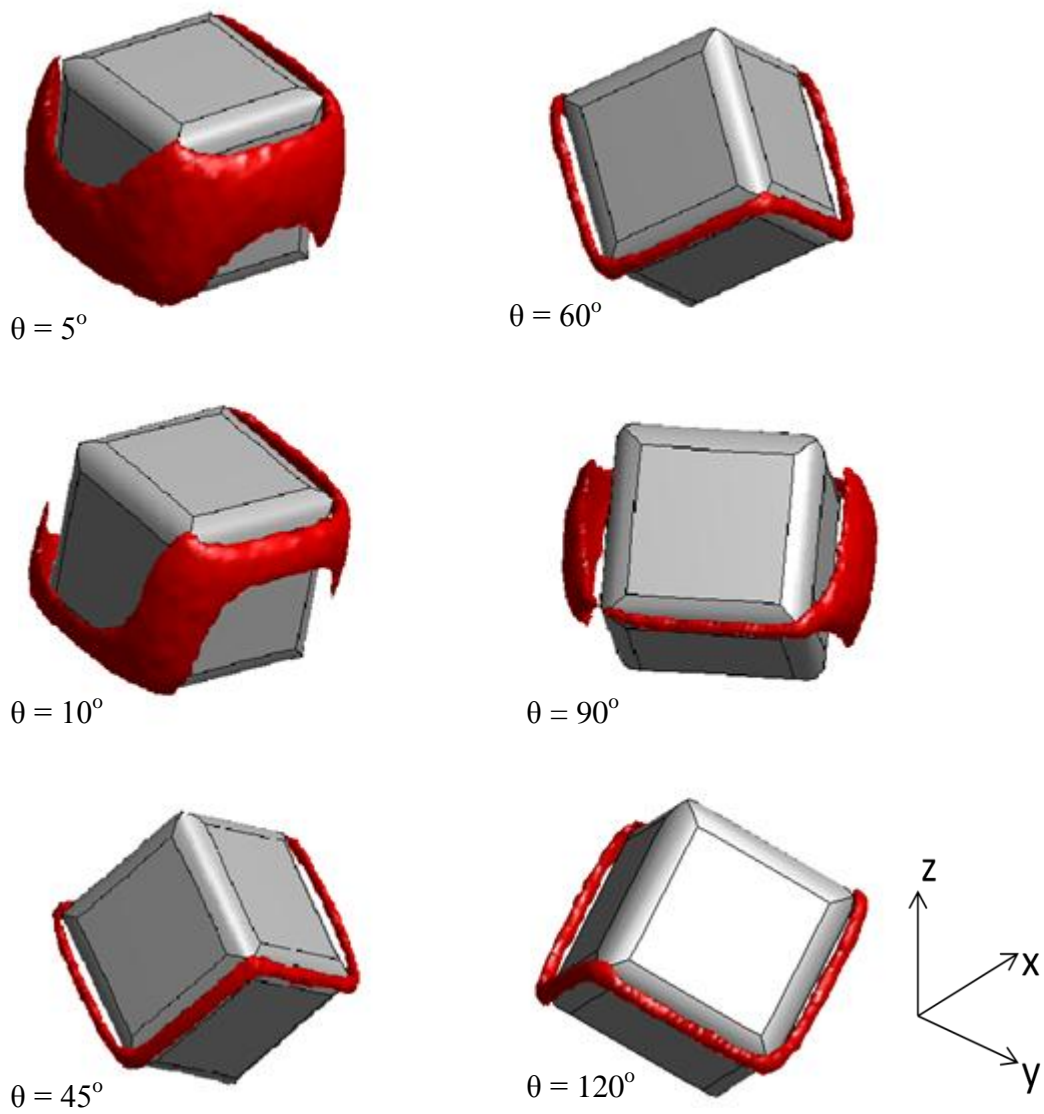


Figure 2.13: 3D visualizations of the NLC distortion around the cubic particle when the particle is rotated around $z=0, x=y$ axis at angle θ .

distortion around the particle over a small interval of angle of rotation (refer [111] and the corresponding 3D visualization in Figure 2.13). Due to the small interval of the angle of rotation, the orientations are close to symmetric configuration ($\theta \sim 0^\circ$) and thus, only a part of distortion gets converted into torque. Hence, due to the rapid decrease in the NLC distortion, we observe a negative torque transmitted by the NLC to the particle (Figure 2.12), instead of a small conventional positive out-of-plane torque. This odd effect might be due to the numerical error.

When a cubic particle orients with its four lateral faces parallel to the far field director $\mathbf{n}(\mathbf{r})$ (i.e. out-of-plane orientations), the torque reaches maximum (see the enclosed light blue rectangular region in Figure 2.12, and the corresponding 3D visualization in Figure 2.13) because NLC around the particle is highly distorted. The magnitude of out-of-plane torques on either side of the stable configuration is similar (Figure 2.12). In case of a cubic particle oriented along the $z=0, x=y$ axis, the stable configuration at $\theta \sim 55^\circ$ is sandwiched between the out-of-plane torques (Figure 2.12). Hence, particle oriented at out-of-plane configuration, with an angle of rotation greater than the stable configuration, would move away from that state and reorient to the stable configuration at $\theta \sim 55^\circ$, more quickly than that of a particle oriented with an angle of rotation smaller than the stable configuration, due to the larger slope (Figure 2.12).

2.2.2.3 Cubic Particle Rotated Around x axis

When a cubic particle is rotated around x axis, the torque profile is divided into three parts: (1) Starting with the zero torque configuration, as the angle of rotation decreases to 30° , we observe in-plane torques similar to Section 2.2.2.1 (Figure 2.14). (2) As the angle of rotation further decreases from $\theta \sim 30^\circ$ to 20° , we observe out-of-plane torques similar to Section 2.2.2.1 (Figure 2.14). (3) As the angle of rotation decrease from $\theta \sim 15^\circ$ to 0° , we observe an unconventional torque similar to Section 2.2.2.2 (Figure 2.14, the corresponding 3D visualization

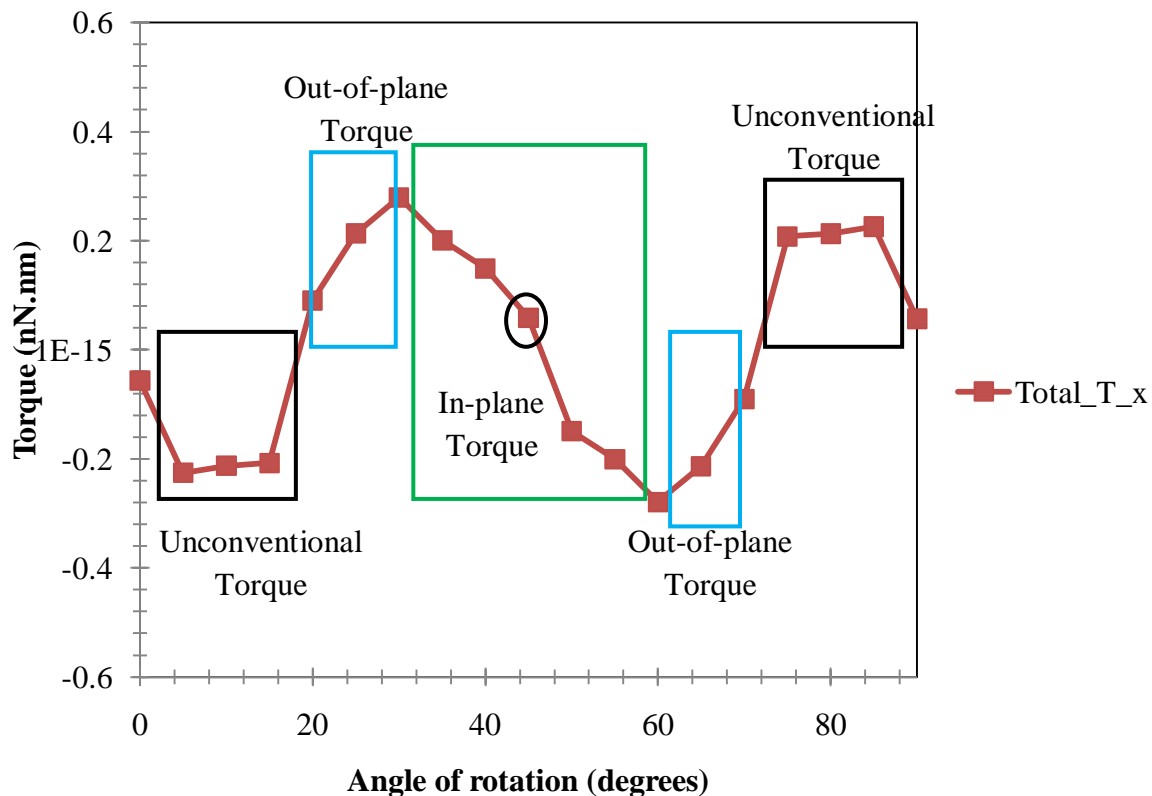


Figure 2.14: Total torque transmitted by the nematic liquid crystal on the one cubic nanoparticle, rotated around the x axis, as a function of angle of rotation. The enclosed blue rectangular region represents angles with out-of-plane rotation, the enclosed green region represents angles with in-plane rotation and the enclosed black region represents angles with unconventional rotation. Circle indicates the most stable and a zero torque configuration.

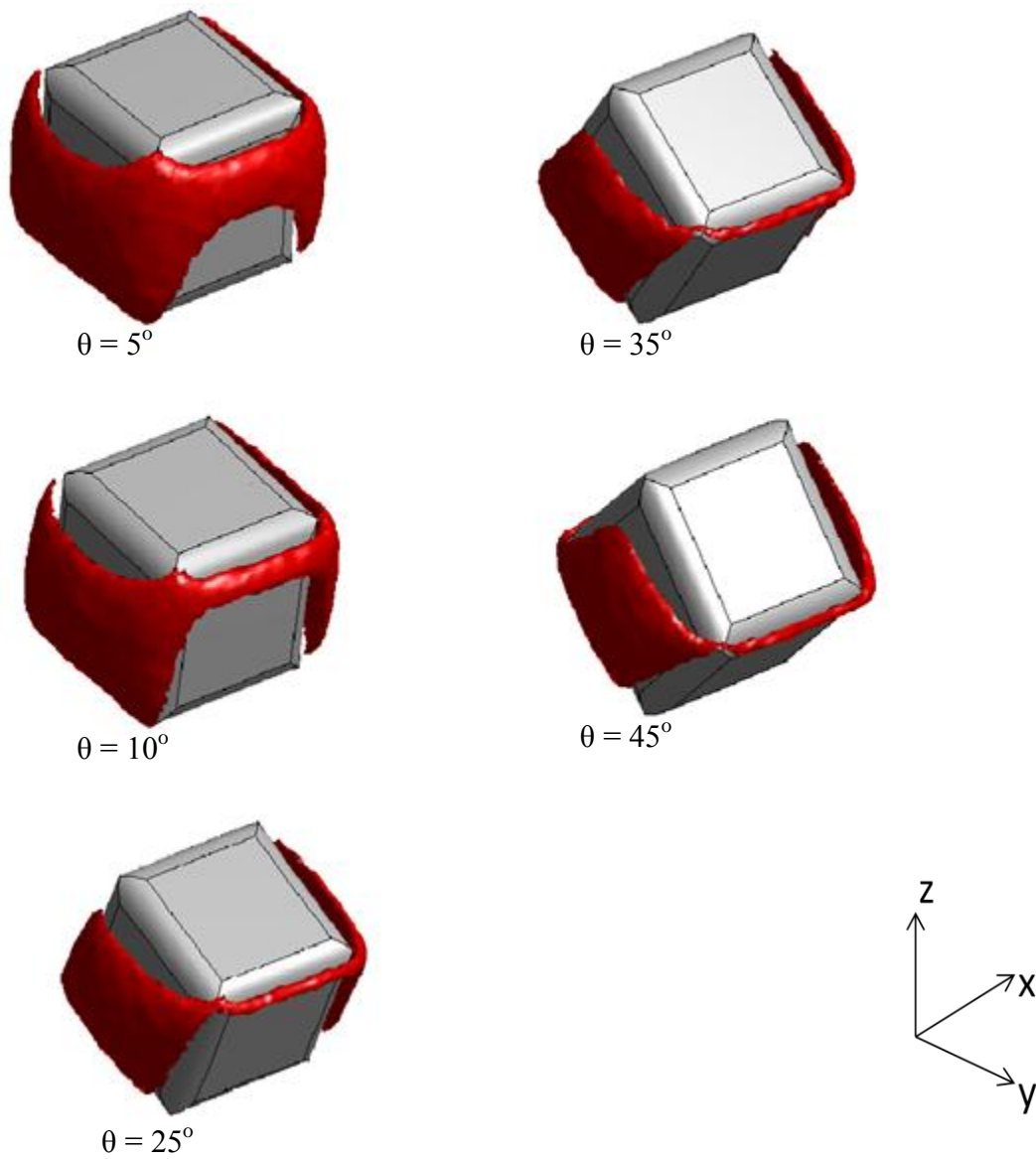


Figure 2.15: 3D visualizations of the NLC distortion around the cubic particle when the particle is rotated around x axis at angle θ .

in Figure 2.15 and refer [111]). A cubic particle oriented along x axis has the most stable and a zero torque configuration at $\theta = 45^\circ$. When a cubic particle orients with its four lateral faces parallel to the far field director $\mathbf{n}(\mathbf{r})$ (i.e. out-of-plane orientations), the torque reaches maximum (see the enclosed blue rectangular region in Figure 2.14, and the corresponding 3D visualization in Figure 2.15) because NLC around the particle is highly distorted. The magnitude of the in-plane torque is similar to that of out-of-plane torque (Figure 2.14). When a cubic particle is oriented around x axis, out-of-plane torque varies more with angle of rotation, due to the larger slope, than the in-plane torque (Figure 2.14), therefore, a cubic particle oriented at unstable configuration (out-of-plane orientations), along the x axis, moves away immediately from that state and then slowly reorients itself to the stable configuration (in-plane orientations).

2.2.2.4. Comparisons

When the particle is oriented at the unstable (out-of-plane) configuration, the total torque (in-plane and out-of-plane) transmitted by the NLC to the particle in order to reorient it to the stable (in-plane) configuration depends on the difference in the NLC distortion around the most unstable and stable configuration. If the difference in the NLC distortion is large, then higher torques is transmitted by the NLC to the particle due to the stronger driving force and vice versa. PMF value represents the stability of the particular orientation (i.e. NLC distortion). The total torque transmitted by the NLC on a cubic particle rotated around the x-axis (Figure 2.14), is nearly four times lower than that on a cubic particle rotated around all the other axes (Figure 2.8, 2.10, and 2.12). This is the axis of rotation effect because, when the particle is rotated around the x-axis only, the difference in the NLC distortion ($\sim 35 k_{\text{BT}}$) around the most unstable (out-of-plane) and stable (in-plane) configuration is smaller than that of a particle rotated around all the

other axes ($\sim 125 \text{ k}_B T$) [111]. Hence, lower torques are transmitted by the NLC on a cubic particle rotated around the x-axis than that around all the other axes.

The torque transmitted by the NLC on a triangular prism shaped particle (Figure 2.3) is nearly twice than that on a cubic particle (Figure 2.8, 2.10, and 2.12). This is a size effect because, in our work, triangular prism particle has more surface area than that of a cubic particle. Thus, the NLC distortion at the most unstable configuration of a triangular prism particle ($\sim 185 \text{ k}_B T$) is higher than that of a cubic particle ($\sim 125 \text{ k}_B T$) [111]. The difference in the NLC distortion around the most unstable and stable configuration is larger for a triangular prism ($\sim 185 \text{ k}_B T$) particle than a cubic particle ($\sim 125 \text{ k}_B T$) [111]. Thus, higher torques are transmitted by the NLC on a triangular prism shaped particle. This demonstrates that, under the possible switching condition with the ratio of size of nanocube and nanoprism similar to this work, a stronger driving force is required to reorient triangular prism shaped particles back to the same stable configurations as compared to cubic particles.

2.2.2.5. Two Cubic Particle System

For two cubic particle systems, torques were calculated for two particles approaching each other with each particle having fixed orientations equal to the thermodynamically stable configuration obtained from the one particle system. Since, according to our previous work for PMF and defect structures [111], several one-particle configurations had similar thermodynamic stability, a configuration, where the cubic nanoparticle is rotated around $z=0$, $x=y$ axes at an angle $\theta = 125^\circ$, is used for two particle systems. We considered two cubic particles approaching in such a way that the defects touch each other and their respective rounded edges are parallel to each other (Figure 2.17). Figure 2.16 shows x, y, and z components of torque transmitted by the NLC to the cubic nanoparticles approaching each other along the x-y plane. Our results indicate

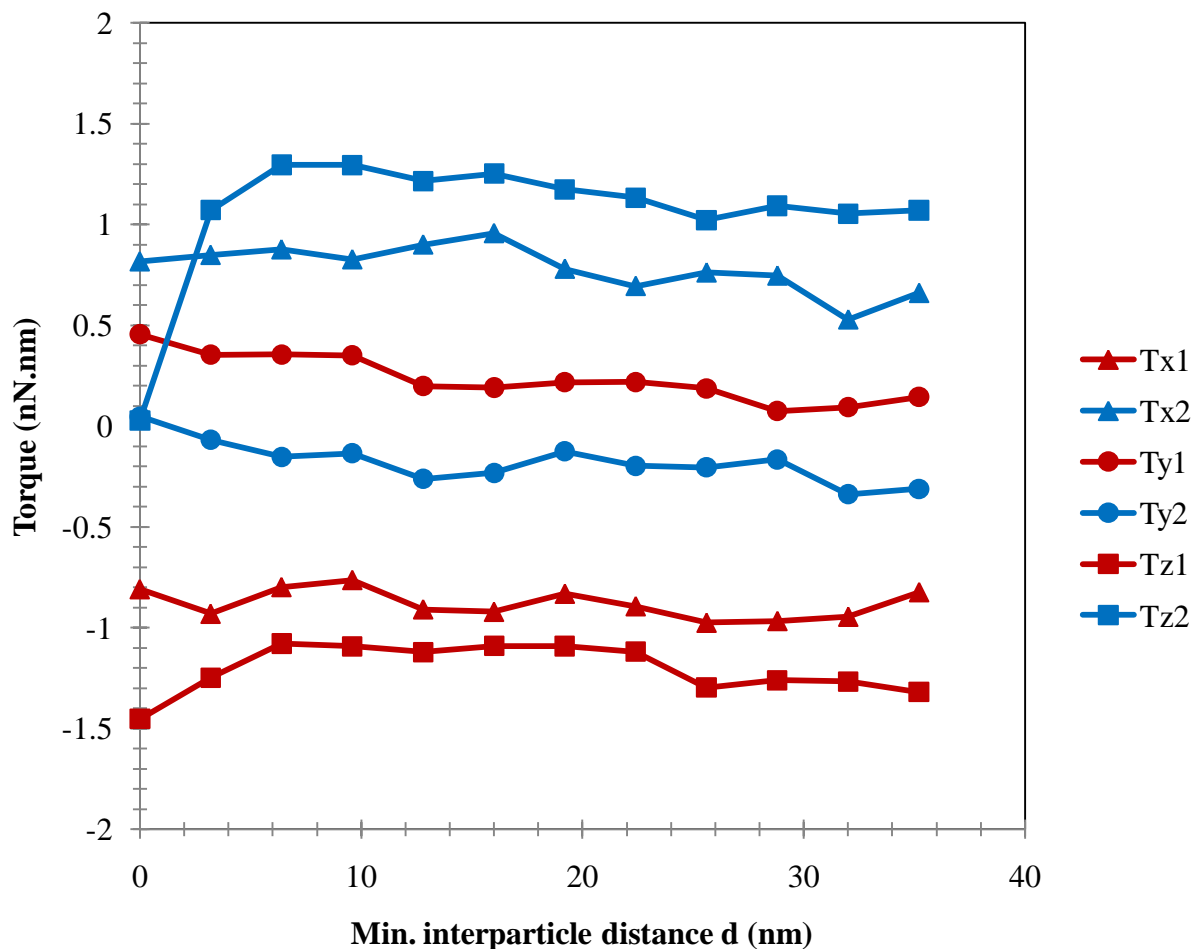


Figure 2.16: Torque transmitted by the nematic liquid crystal on the two cubic particle system as a function of minimum surface-to-surface interparticle distance d . Triangles: x component of torque acting over particle 1 (red) and 2 (blue). Circles: y component of torque acting over particle 1 (red) and 2 (blue). Squares: z component of torque acting over particle 1 (red) and 2 (blue).

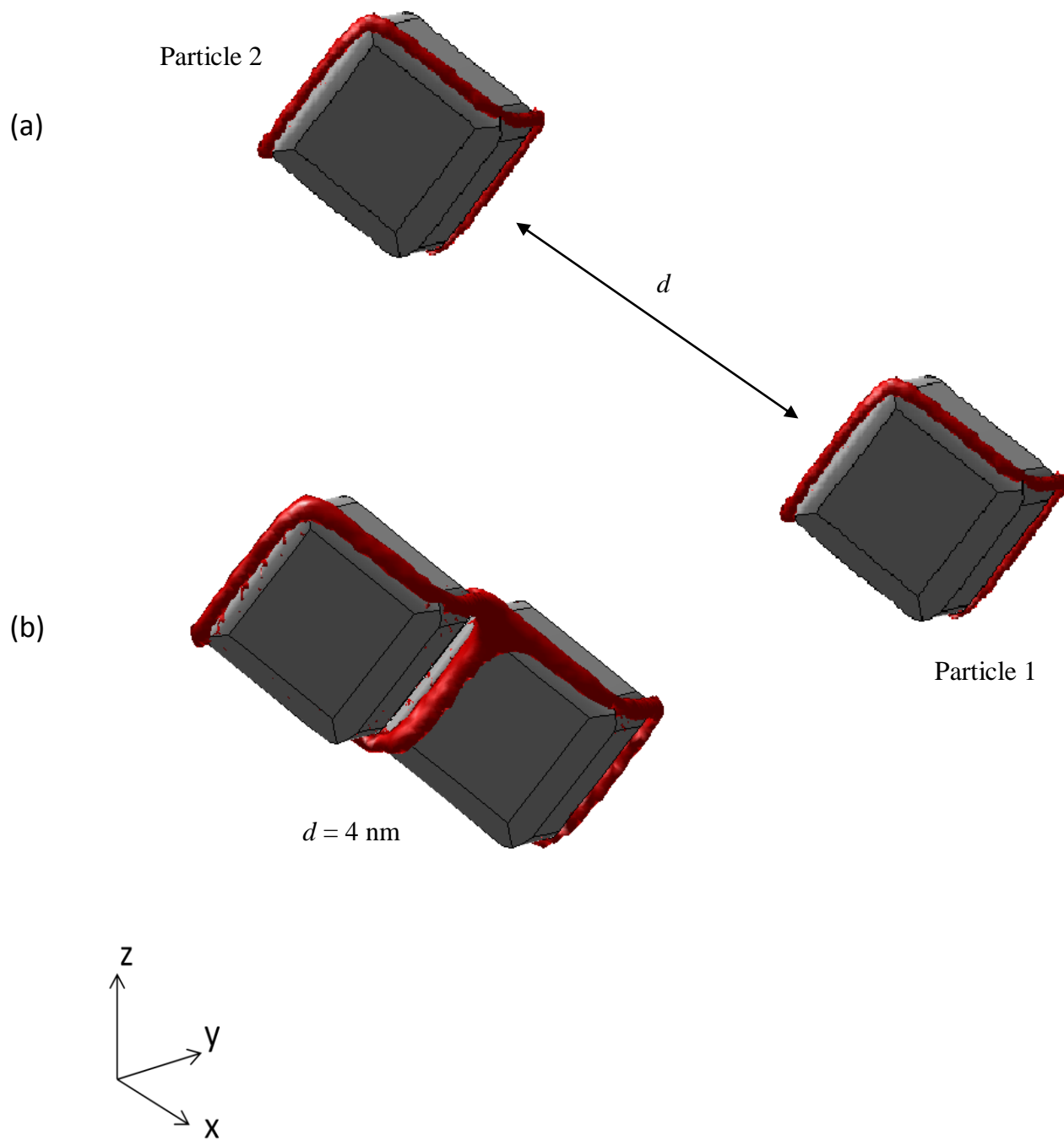


Figure 2.17: (a) Schematic representation of two cubic particles approaching each other through the interparticle distance d . (b) 3D visualizations of the defect structure formed by a nematic liquid crystal around the two cubic particles separated by the interparticle distance $d = 4$ nm.

that z component of the torque transmitted by the NLC to the cubic particles ($T_{z(1,2)}$) is more significant than the x ($T_{x(1,2)}$) and y ($T_{y(1,2)}$) component of the torque for all the interparticle distances considered. The x, y and z components of torque for both the cubic particles approaching each other T_x , T_y and $T_z \neq 0$ even at a distance $d > 30\text{nm}$. This behavior is observed because a cubic particle oriented around $z=0$, $x=y$ axes at an angle $\theta = 125^\circ$ has thermodynamic stability due to the lowest surface area of the defect structure around the particle (i.e. least NLC distortion) but it does not have a zero torque. For zero torque configurations, the defect structure around the configuration should have a high degree of symmetry (i.e. balanced NLC distortion) along with low surface area.

The x, y and z components of torque on both the cubic particles have opposite signs because both cubic particles approach each other through different octant domains of the coordinate system. The cubic particle 1 is in bottom-back-right octant whereas the cubic particle 2 is in top-front-left octant (Figure 2.17). As compared to triangular prism shaped particles system, there is no significant change in the components of torque for both cubic particles till $d \sim 6 \text{ nm}$ (Figure 2.16) and the repulsion is not as significant because the cubic particles approach with edges (none of the faces) parallel to each other (Figure 2.17). According to our previous work [111], stable nanocubes prefer to be close to each other ($d \sim 5 \text{ nm}$) because the surface area of the NLC distortion around the particles is the smallest. Due to their trajectory of approach along the x-y plane, as the interparticle distance decreases from $d \sim 6 \text{ nm}$ to 0 nm , the repulsion between the particles produces the significant change in the z and y component of torque whereas the x component of torque remains constant. Hence, when the interparticle distance decreases from $d \sim 6 \text{ nm}$ to 0 nm , the negative z component of torque T_{z1} on cubic particle 1 increases from $\sim -1.1 \text{ nN.nm}$ to $\sim -1.5 \text{ nN.nm}$ whereas the positive z component of torque T_{z2} on

cubic particle 2 decreases from ~ 1.25 nN.nm to ~ 0 nN.nm (Figure 2.16). Similarly, the positive y component of torque T_{y1} on cubic particle 1 increases from ~ 0.3 nN.nm to ~ 0.45 nN.nm whereas the negative y component of torque T_{y2} on cubic particle 2 decreases from ~ -0.2 nN.nm to ~ 0 nN.nm (Figure 2.16). Our torque results for one cubic particle systems suggest that the total torque on the cubic particle oriented around $z=0, x=y$ axes at an angle $\theta = 125^\circ$ is non-zero therefore, the repulsion, at $d < 6$ nm, pushes cubic particle 1 in its original path and increases the magnitude of the z and y component of torque on cubic particle 1. However, the repulsion, at $d < 6$ nm, pushes cubic particle 2 against its original path and decreases the magnitude of the z and y component of torque on cubic particle 2 to zero.

When the particles are close to each other ($d \sim 5$ nm), the total torque on each triangular prism shaped particle (~ 3.5 nN.nm), due to the presence of their respective particle, is higher than that on a cubic particle (~ 2 nN.nm) (Figure 2.6 and 2.16). This difference is due to the fact that triangular prism particles approach with their rectangular faces parallel to each other whereas the cubic particles approach with their edges parallel to each other (Figure 2.7 and 2.17). The rectangular face of the triangular prism has more surface area than the edge of the cube and hence, when the particles are close to each other, the force applied by the intervening NLC to the triangular prism particles would be higher and in turn develops higher torques.

2.3. Concluding Remarks

We investigated torques transmitted by the NLC to the faceted particle, namely cubic and equilateral triangular prism shaped particle, in order to analyze the reorientational behavior of a faceted particle to the stable (minimum distortion) configuration. For one particle system, the torque profile was mainly divided into two parts: (1) in-plane torques and (2) out-of-plane torques, except when a cubic particle was oriented along $z=0, x=y$ axis where the torque profile

has only out-of-plane torques. The magnitude of the out-of-plane torque is similar to that of in-plane torque but their variation with respect to the angle of rotation differs. Mostly, out-of-plane torque varies more than in-plane torques with respect to the angle of rotation due to their large slope. These out-of-plane orientations are unstable configurations and when a particle is oriented at these configurations, it immediately moves away from that state, which is evident by the large slope, and then it slowly reorients itself to the closest stable configuration. In the torque profile, generally, the stable configuration also has the zero torque except when a cubic particle was oriented along $z=0$, $x=y$ axis. In order to have a zero torque, a configuration should have high degree of symmetry along with low surface area of NLC distortion around it.

In case of equilateral triangular prism shaped particle system, the torque reaches maximum when the particle orients with one of its rectangular sides parallel to the far field director $\mathbf{n}(\mathbf{r})$ (i.e. out-of-plane orientations). Whereas, in case of cubic particle, the torque reaches maximum when the particle orients with its four lateral faces parallel to the far field director $\mathbf{n}(\mathbf{r})$ (i.e. out-of-plane orientations). Our results suggests that the torque transmitted by the NLC on a cubic particle rotated around the x-axis (Figure 2.14), is nearly five times lower than that on a cubic particle rotated around all the other axes (Figure 2.8, 2.10, and 2.12) due to the axis of rotation affect. Our results also indicate that, due to the size effect, the torque transmitted by the NLC on a triangular prism shaped particle (Figure 2.3) is nearly twice than that on a cubic particle (Figure 2.8, 2.10, and 2.12). Thus, under the possible switching condition with the ratio of size of nanocube and nanoprism similar to our work, a stronger driving force is required to reorient triangular prism shaped particles back to their stable configurations as compared to cubic particles.

For two-particle system, depending upon the plane along which the particles approach each other, one component of torque is significant than the other two components. From this study, it is observed that, when two particles are close to each other, the NLC transmits more torque on the stable triangular nanoprism, due to the presence of their respective particle, than that on stable nanocube (Figure 2.6 and 2.16). This difference in the magnitude of torque occurs because the cubic particles approach with their edges (none of their faces) parallel to each other whereas, the triangular prism particles approach with their rectangular faces parallel to each other (Figure 2.7 and 2.17). It is known that the magnitude of the torques on the particles can be reduced to some extent by making them approach each other via 'diagonal' trajectory.

CHAPTER 3. MOLECULAR DYNAMICS SIMULATION OF SYSTEMS OF CARBON NANOTUBES AND LIQUID CRYSTALS

3.1. Simulation Details

The system consist of a rectangular box of dimensions L_x , L_y and L_z , containing two CNTs separated by a distance d and immersed in a liquid crystalline solvent (Figure 3.1). Periodic boundary conditions are applied in all the three directions (x , y and z). LCs with different chemical structure: 5CB and 8CB (which are members of the 4-cyano-4'-n-alkylbiphenyl series (nCB)) (Figure 3.2) and different phases: smectic and nematic phase of 8CB LC, were considered in these simulations (Figure 1.1). Regarding the CNTs, single-walled CNTs with armchair configuration (5, 5) are considered in our simulations. GROMACS MD software is used to perform our simulations [124]. The *.gro* file for each molecule was generated using the PRODRG server [125]. The *.gro* file for the carbon nanotube was generated using the software Nanotube Modeler JCrystalSoft [126]. The topology file for each molecule was generated using GROMACS utility *x2top*. The initial configurations of our systems were generated using the GROMACS utilities *genconf* and *editconf*. The VMD [127] software was used for all our visualizations. The AMBER unified-atom force field was used to model 8CB and 5CB [128].

The initial configurations were first relaxed using an energy minimization procedure using the steepest descent method. Afterwards, MD simulations were performed in the isothermal-isobaric ensemble (NPT), at atmospheric pressure and at temperatures where the LC is either in the nematic or isotropic phase. In order to understand the molecular-level interactions between the CNTs and the LCs, we carried out both the potential of mean force (PMF) calculations and conventional MD simulations. The PMF calculations provide the free energy profile for two CNTs moving close to each other through a given LC solvent. The constraint force method is used for our simulations [129-132]. In constraint force simulations, the distance

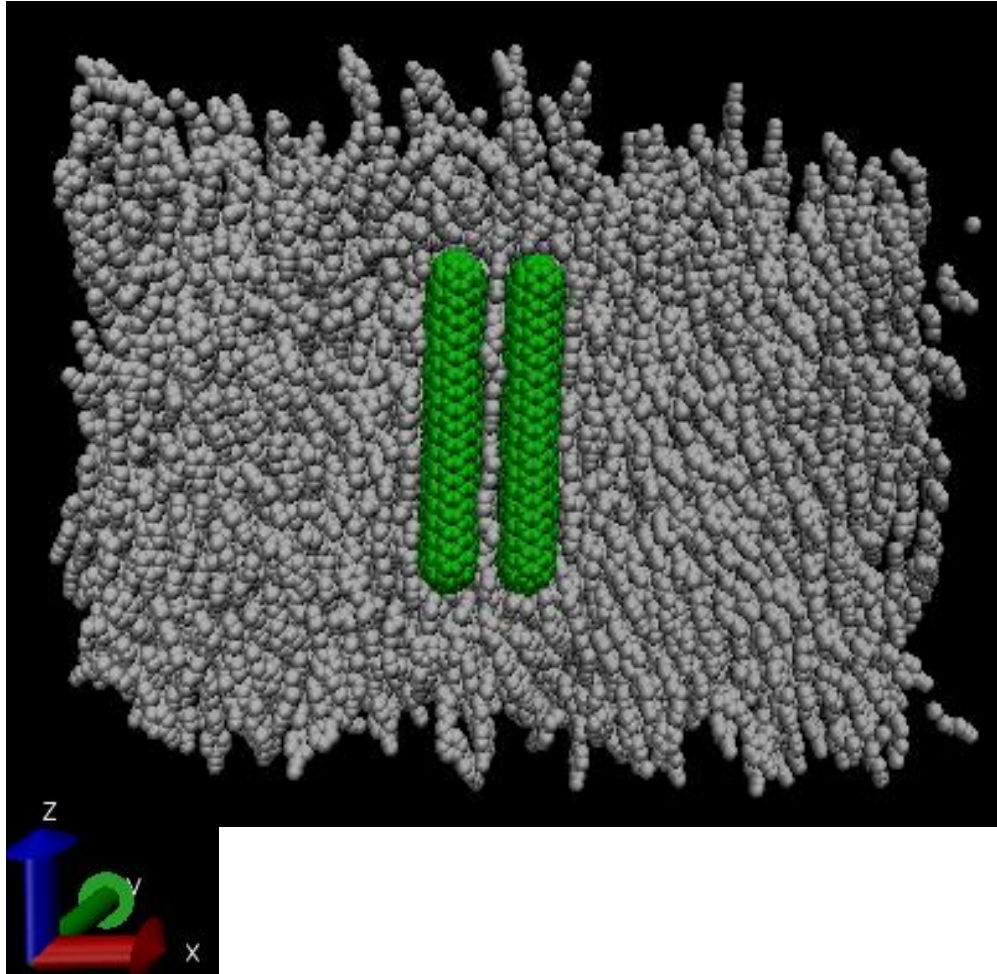
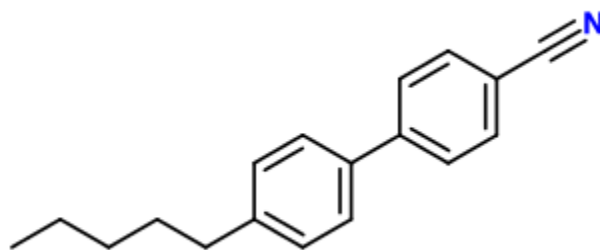
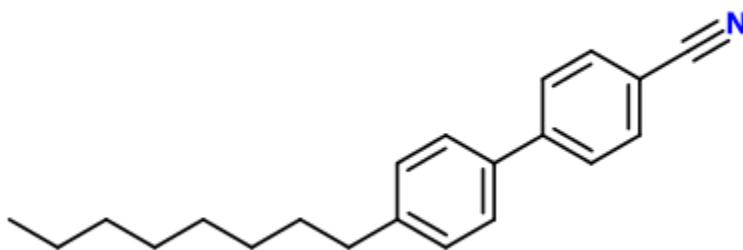


Figure 3.1: Representative simulation snapshot of an MD simulation of a system of two CNTs immersed in 5CB in the nematic phase.



5CB



8CB

Figure 3.2: The molecular structure of 5CB and 8CB LC. 8CB LC has three more carbon atoms in the hydrophobic part of the molecule than 5CB LC.

between the center of mass of two carbon nanotubes are constrained in x-direction. The force required to constraint two CNTs in the system at the fixed distance was calculated during the simulations. Once the constraint force MD simulations were performed at a range of distance (d) between the CNTs, the potential of mean force (PMF) was obtained by integrating these forces [129-132] with respect to a reference point, whose free energy value is assigned to zero. In this study, the reference point is the state where the two carbon nanotubes are far apart. In order to calculate PMF, constraint force MD simulations are performed at distance (d) ranging from 0 to 2 nm with an interval of 0.0625 nm. Simulations were run for 8 ns and at least 6 ns of the equilibrated production runs were used to calculate the PMF. The PMF was determined as a function of the distance d between the two CNTs.

3.2. Results and Discussions

3.2.1. Investigating the Interactions between the CNTs in 5CB and 8CB Nematic Liquid Crystal System

The interactions between the CNTs in LCs were investigated with two armchair single-walled CNT (5, 5) and, 5CB and 8CB NLCs (members of the 4-cyano-4'-n-alkylbiphenyl series (nCB)). Figure 3.1 shows representative simulation snapshot of an MD simulation of a system of two CNTs immersed in 5CB NLCs. The difference in the 5CB and 8CB LC is the chain length of the hydrophobic part of the LC molecule. 8CB LC has three more carbon atoms in the hydrophobic part of the molecule than 5CB LC (Figure 3.2). Our objective is to find how the interactions between the CNTs are affected by varying the chain length of the hydrophobic part of nCB LC. MD simulations were performed in the isothermal-isobaric ensemble (NPT), at atmospheric pressure and at temperatures where the LC is in the nematic phase. Periodic boundary conditions are applied in all the three directions (x, y and z).

Figure 3.3 shows the calculated PMF, for the system of CNTs immersed in the 5CB and 8CB NLCs, as a function of the fixed distance d between the CNTs. The PMF profiles have deepest minima at $d \sim 0.25$ nm for 5CB and 8CB NLCs system. This minimum is referred to as the contact minimum (CM) (Figure 3.7(a)) [95]. The CM determines the CNT's preference to come in contact with each other. The CM for 5CB NLCs (~ -13.4 kcal/mol) is deeper than that of 8CB NLCs system (~ -11.5 kcal/mol). This indicates that the CNTs will have strong tendency of aggregation in 5CB NLCs system than that in 8CB NLCs system. The maximum in the PMF profile after the contact minima is referred to as the desolvation maximum (DM) (Figure 3.7(b)) [95]. The DM for both NLCs system has the same the PMF value (~ 0.5 kcal/mol) and occurs at $d \sim 0.45$ nm. The DM occurs because of the unfavorable free energy of the system caused by NLCs trying to form a single layer of NLCs between the CNTs (Figure 3.8(a)). The PMF profiles have the second minima referred to as solvent-separated minima (SSM) [95] at $d \sim 0.63$ nm for 5CB and 8CB NLCs system (Figure 3.7(c)). SSM determines the CNT's preference to be separated by a single layer of solvent. The SSM is deeper for 5CB NLC (~ -6.2 kcal/mol) than that of 8CB NLC system (~ -4.6 kcal/mol). This depth of the SSM indicates that the CNTs would prefer to be separated by a single layer of 5CB NLC as compared to a single layer of 8CB NLC.

The PMF profiles have the second maxima referred to as second desolvation maximum (SDM) (Figure 3.7(d)). The SDM occurs because of the unfavorable free energy of the system caused by NLCs trying to form two layers of NLCs between the CNTs (Figure 3.8(b)). The SDM for both NLCs system occur at $d \sim 0.85$ nm but SDM is deeper for 5CB NLC (~ -3.4 kcal/mol) than that of 8CB NLC system (~ 1.0 kcal/mol). The minimum after the SDM is referred to as third minima (TM) (Figure 3.7(e)) [95]. TM determines the CNT's preference to be separated by two layers of solvent. The TM for both NLCs system occurs at $d \sim 0.95$ nm but TM is deeper for

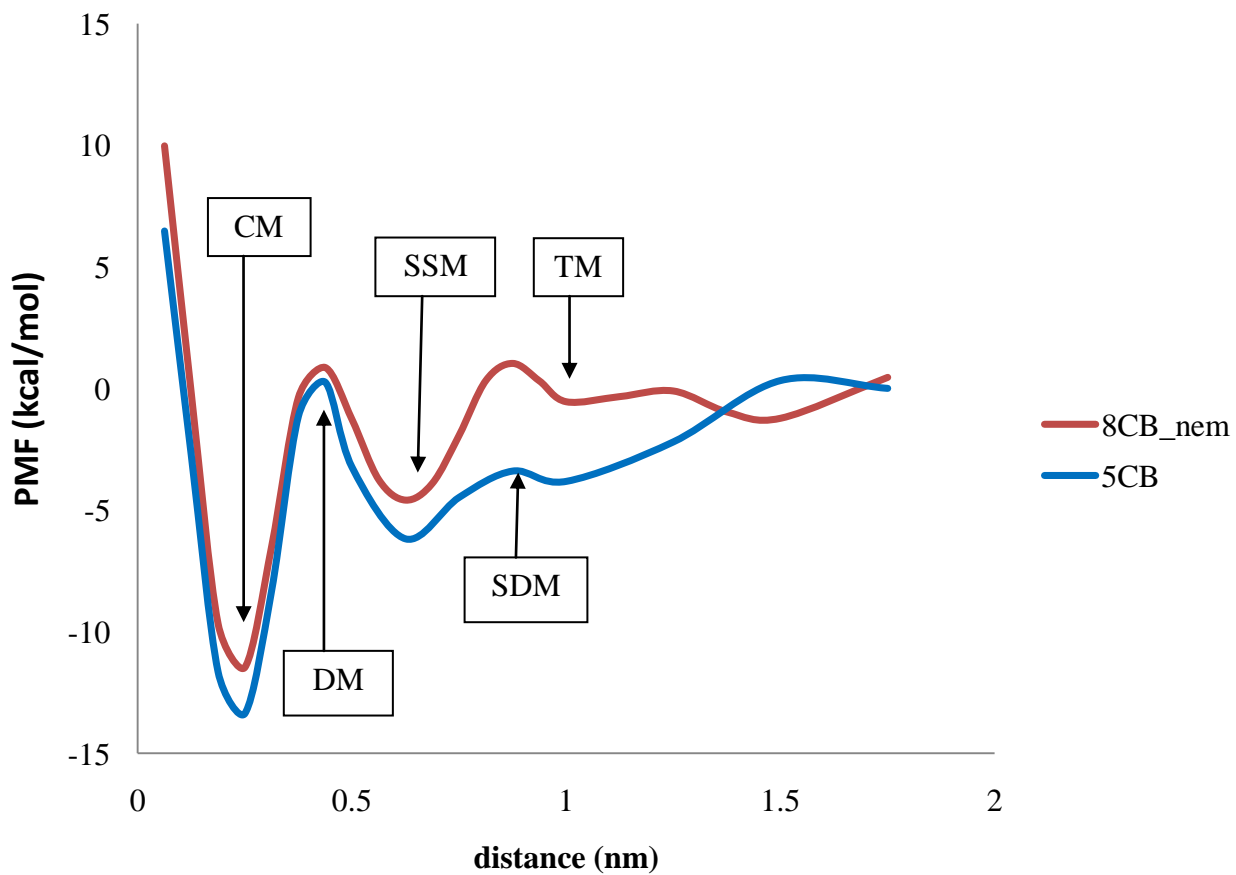


Figure 3.3: The calculated PMF, for the system of CNTs immersed in the 5CB and 8CB NLCs, as a function of the fixed distance d between the CNTs.

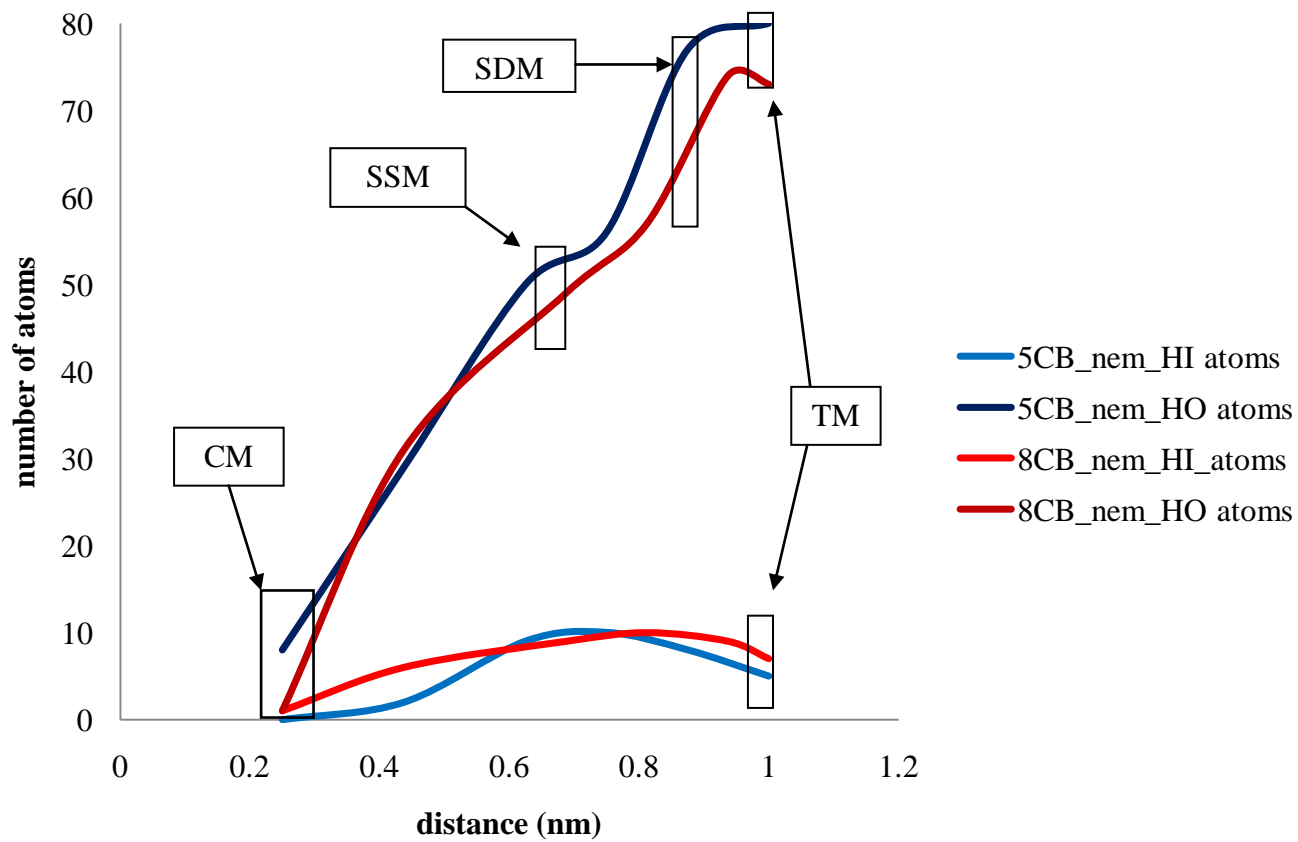


Figure 3.4: Number of hydrophobic (HO) and hydrophilic (HI) atoms of 5CB and 8CB NLCs in the volume between the CNTs, as a function of fixed distance d .

5CB NLC (~ -3.8 kcal/mol) than that of 8CB NLC system (~ -0.6 kcal/mol). This depth of the TM indicates that the CNTs would prefer to be separated by two layer of 5CB NLC as compared to that of 8CB NLC.

Figure 3.4 shows number of hydrophobic (HO) and hydrophilic (HI) atoms of 5CB and 8CB NLC in the volume between the CNTs, as a function of fixed distance d . Figure 3.4 is the representative of the concentration of hydrophobic and hydrophilic part of 5CB and 8CB NLC in the volume between the CNTs. The CM, SSM and TM for 5CB NLCs system are much deeper than that of 8CB NLCs system (Figure 3.3). This difference in the depth is most likely due to the difference in the hydrophobicity between the CNTs (depending on the number of hydrophobic and hydrophilic atoms between the CNTs). It is for this precise reason that, we calculated the number of hydrophobic and hydrophilic atoms in the volume between the CNTs, as a function of fixed distance, which is presented in Figure 3.4. At CM ($d \sim 0.25$ nm) and SSM ($d \sim 0.63$ nm), in the volume between the CNTs, there are more number of hydrophobic atoms for 5CB NLC system as compared to that of 8CB NLC system (Figure 3.4). Hence, the attraction between the hydrophobic CNTs increases and thus, the CM, and SSM are deeper for 5CB NLCs system than that of 8CB NLCs system (Figure 3.3). As the distance between the CNTs increases further from $d \sim 0.8$ nm, there is an increase in the number of hydrophobic atoms and decrease in the number of hydrophilic atoms for the 5CB NLC system as compared to the 8CB NLC system (Figure 3.4). Thus, at SDM ($d \sim 0.85$ nm), there is an increased attraction between the CNTs and, as compared to the separations $d < 0.8$ nm, the PMF is deeper for 5CB NLC system than that of 8CB NLC system (Figure 3.3). At TM ($d \sim 0.95$ nm), the difference in the number of hydrophobic atoms for both the systems is smaller than that at SDM and thus, the difference in the PMF at TM is smaller than that at SDM (Figure 3.3). However, at TM, 5CB NLCs system has more number of

hydrophobic atoms and less number of hydrophilic atoms as compared to that of 8CB NLCs system (Figure 3.4). Thus, TM is deeper for 5CB NLCs system than that of 8CB NLCs system (Figure 3.3).

At larger separation d , the PMF reaches a value of 0 as the interaction between the CNTs becomes sluggish, since the stable layers of NLCs are formed between the CNTs. As the PMF for the 5CB NLCs system reaches a value of 0 at a separation ($d \sim 2.0$ nm) larger than that of 8CB NLCs ($d \sim 1$ nm) system (Figure 3.3), there is a strong attraction between the CNTs in the 5CB NLCs system as compared to the 8CB NLCs system. The CM for 5CB NLCs is deeper than that of 8CB NLCs system and there is a significant difference in the PMF profiles. This indicates that, increasing the chain length of the hydrophobic tail of the nCB LC molecule decreases the tendency of aggregation for CNTs in nCB LCs.

3.2.2. Investigating the Interactions between the CNTs in 8CB Nematic and Smectic Liquid Crystal System

The interactions between the CNTs in LCs were investigated with two armchair single-walled CNT (5, 5) and, 8CB nematic and smectic LCs (member of the 4-cyano-4'-n-alkylbiphenyl series (nCB)). The density of the 8CB smectic phase (~ 1010 g/m³) is higher than that of the nematic phase (~ 985 g/m³) because of its positional order (Figure 1.1). Figure 3.5 shows the calculated PMF, for a system of CNTs immersed in two different phases of 8CB LC, as a function of the fixed distance d between the CNTs. The CM for 8CB NLCs and SLCs occurs at $d \sim 0.25$ nm and has nearly the same depth (~ -12 kcal/mol) which indicates that the CNTs will have the same tendency of aggregation in 8CB NLCs and SLCs system. The DM for both the phases has nearly the same PMF value (~ 1.5 kcal/mol) and occurs at $d \sim 0.45$ nm. The SSM for 8CB NLCs and SLCs occurs at $d \sim 0.63$ nm and has the same depth (~ -0.42 kcal/mol) which indicates that the CNTs would have same preference to be separated by a single layer of 8CB

NLC and SLC. The SDM for both the phases has nearly the same PMF value (~ 0.5 kcal/mol) and occurs at $d \sim 0.85$ nm. The TM for both the phases occurs at same position $d \sim 0.95$ nm but the TM for 8CB SLCs (~ -2.9 kcal/mol) is deeper than the 8CB NLCs system (~ -0.6 kcal/mol). This indicates that the CNTs would prefer to be separated by two layers of 8CB SLCs as compared to the 8CB NLCs.

Figure 3.6 shows number of hydrophobic (HO) and hydrophilic (HI) atoms of 8CB NLC and SLC in the volume between the CNTs, as a function of fixed distance d . Figure 3.6 is the representative of the concentration of hydrophobic and hydrophilic part of 8CB NLC and SLC in the volume between the CNTs. There is no significant difference in the PMF profiles for 8CB NLCs and SLCs at shorter separations ($d < 0.85$ nm). This occurs because both the phase systems have nearly the same hydrophobicity, which depends upon the number of hydrophobic and hydrophilic atoms in the volume between the CNTs (Figure 3.6). As the distance between the CNTs increases from $d \sim 0.85$ nm, there is an increase in the number of hydrophobic atoms in the 8CB SLC system as compared to the 8CB NLC system (Figure 3.6). Thus, at TM ($d \sim 0.95$ nm), there are more number of hydrophobic atoms in the 8CB SLCs system as compared to 8CB NLCs system (Figure 3.6). Due to this reason, we observe that the TM is deeper for 8CB SLCs system than that of 8CB NLCs system (Figure 3.5). Figure 3.7 shows the representative simulation snapshot of the (a) CM, (b) DM (c) SSM (d) DSM and (e) TM configuration for a system of two CNTs immersed in the 8CB SLCs. Figure 3.8 shows the front view of the DM and SDM configuration for a system of two CNTs immersed in the 8CB SLCs.

However, the PMF for both the phase system reaches a value of 0 as the interaction between the CNTs becomes sluggish, because the stable layers of NLCs are formed between the CNTs (Figure 3.5). The CM for 8CB NLCs and SLCs has the same depth and there is a

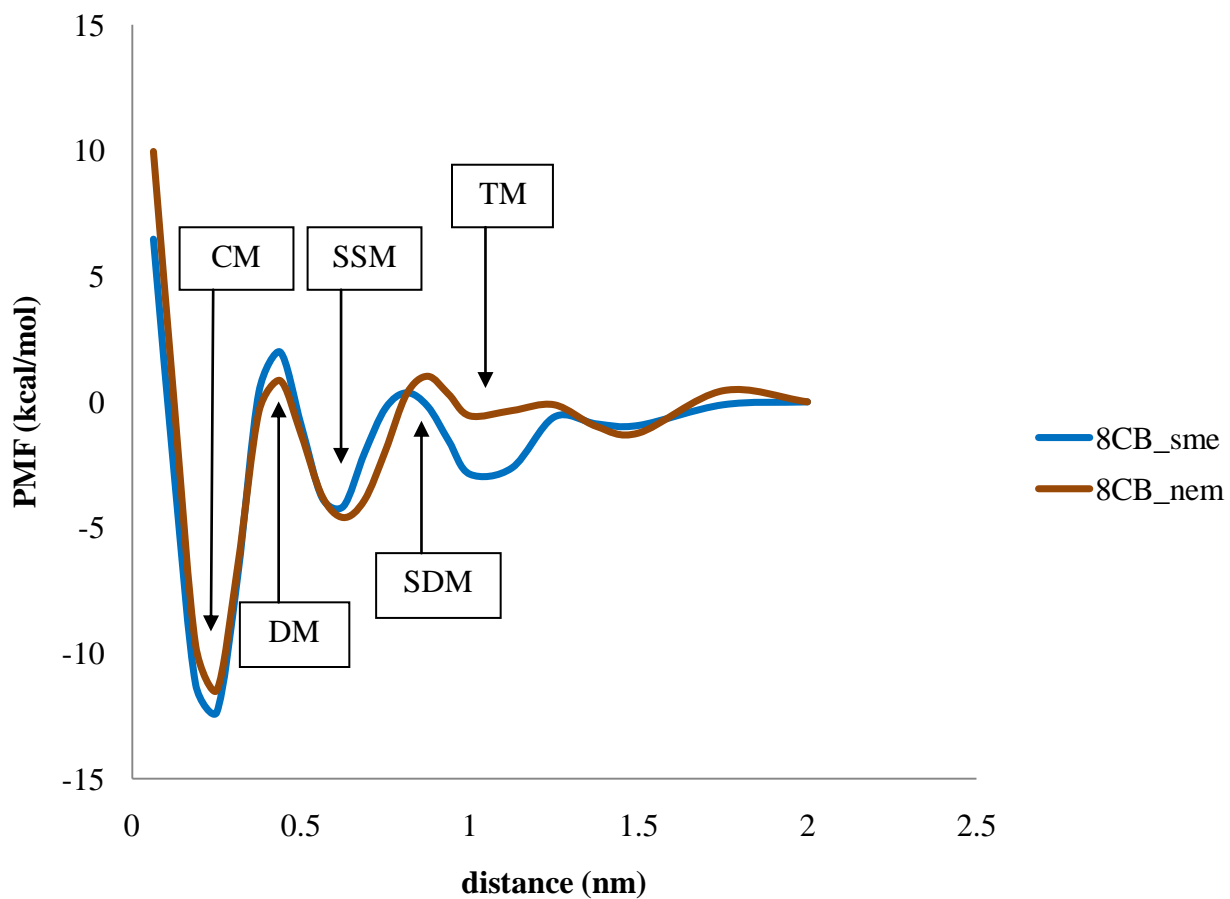


Figure 3.5: The calculated PMF, for the system of CNTs immersed in the 8CB NLCs and SLCs, as a function of the fixed distance d between the CNTs.

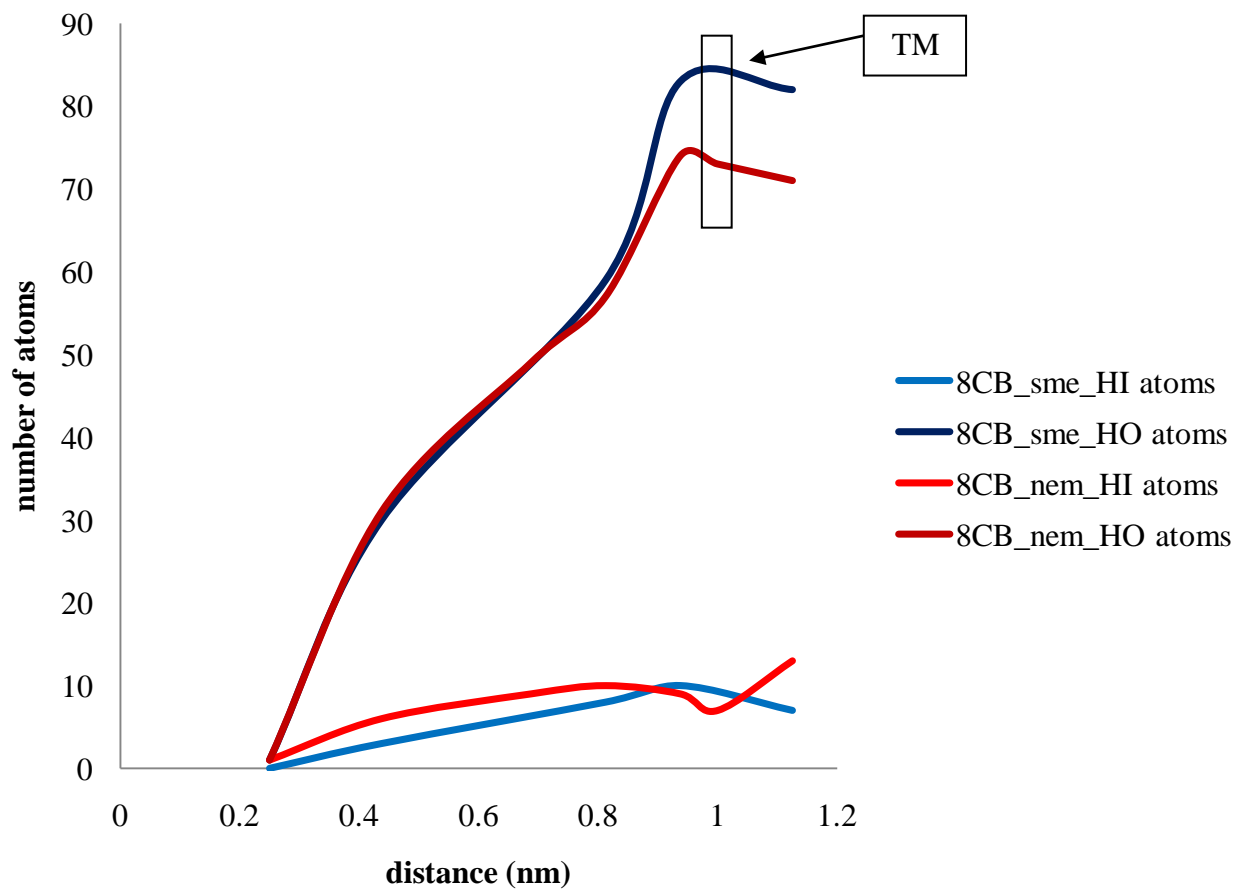


Figure 3.6: Number of hydrophobic (HO) and hydrophilic (HI) atoms of 8CB NLCs and SLCs in the volume between the CNTs, as a function of fixed distance d .

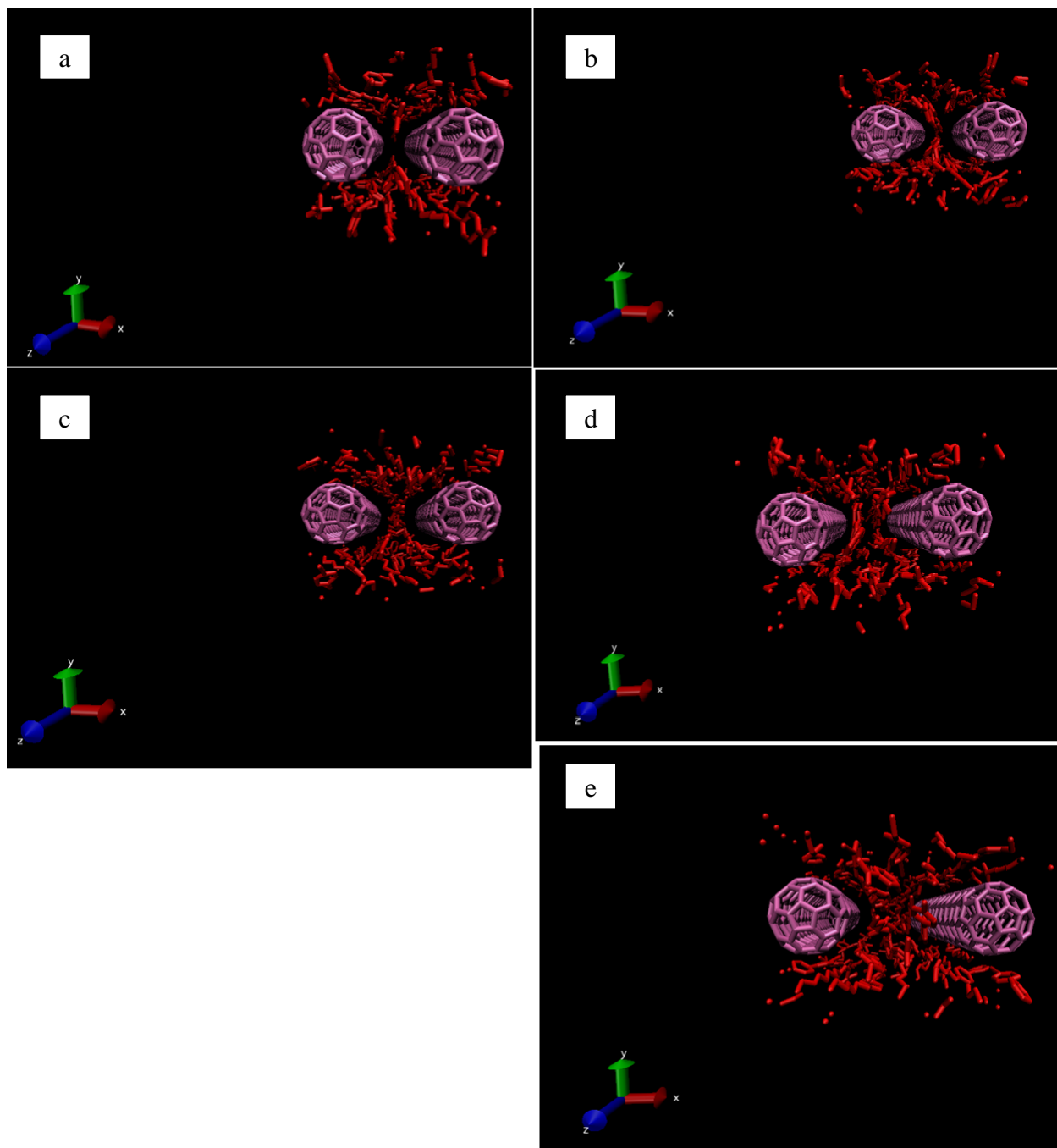


Figure 3.7: The simulation snapshot of (a) CM, (b) DM (c) SSM (d) SDM and (e) TM configuration for a system of two CNTs immersed in the 8CB SLCs.

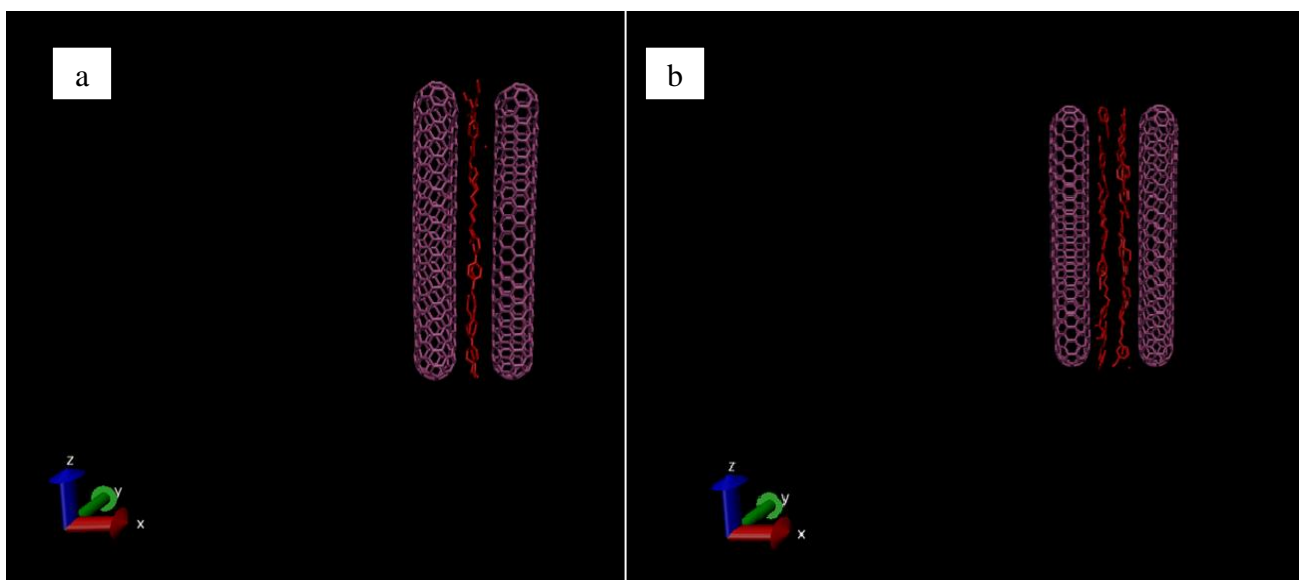


Figure 3.8: Front view of the simulation snapshot of (a) DM and (b) SDM configuration for a system of two CNTs immersed in the 8CB SLCs.

significant difference in the PMF profiles only for small range of separation ($d \sim 0.85$ to 1.2 nm). This indicates that varying the phase of the liquid crystalline solvent is insufficient to decrease the tendency of aggregation for CNTs in nCB LCs.

3.3. Concluding Remarks

Molecular dynamics simulations were performed to investigate the interactions between the CNTs immersed in the liquid crystalline solvent. Our objective was to investigate how the interactions between the CNTs in liquid crystalline solvent are affected by varying the molecular structure and the phase of the LC. The interactions between the CNTs in 5CB and 8CB NLCs system were investigated in order to understand the effect of varying the chain length of the hydrophobic part of the nCB LC molecule on the CNTs interactions. 8CB LC has three more carbon atoms in the hydrophobic part of the molecule than 5CB LC (Figure 3.2). Our results indicate that the CNTs would prefer to be separated by one and two layers of 5CB NLC than that of 8CB NLC. The CM for 5CB NLCs is deeper than that of 8CB NLCs system and the PMF for the 5CB NLCs system reaches a value of 0 at larger separation than that of 8CB NLCs system (Figure 3.3). This indicates that, there is a strong tendency of aggregation for CNTs in the 5CB NLCs system as compared to the 8CB NLCs system. Thus, increasing the chain length of the hydrophobic part of the nCB LC molecule decreases the tendency of aggregation for CNTs in nCB LCs.

The interactions between the CNTs in 8CB NLCs and SLCs system were investigated in order to understand the effect of varying the phase of the liquid crystalline solvent on the CNTs interactions. The density of the 8CB smectic phase (~ 1010 g/m³) is higher than that of the nematic phase (~ 985 g/m³) because of its positional order (Figure 1.1). Our results indicate that the CNT's preference to be separated by a single layer of 8CB NLC and SLC would be similar

however; they would prefer to be separated by two layers of 8CB SLC than that of 8CB NLC. The CM for 8CB NLCs and SLCs has the same depth and there is a significant difference in the PMF profiles only for small range of separation (Figure 3.5). This demonstrates that, the tendency of aggregation for CNTs is similar in 8CB NLCs and SLCs system. Thus, varying the phase of the liquid crystalline solvent is insufficient to decrease the tendency of aggregation for CNTs in nCB LCs.

CHAPTER 4. CONCLUSIONS AND FUTURE DIRECTIONS

In this work, the use of liquid crystal to manipulate and organize the faceted nanoparticles and carbon nanotubes (CNTs) was investigated. The research was divided into two independent but directly related projects. In first part of the research, we performed mesoscale simulations of faceted nanoparticles in nematic liquid crystal (NLC) in order to investigate the torques that develop when faceted nanoparticles, namely cubes and triangular prisms, are immersed in a nematic LC. Torques were investigated in order to analyze the reorientational behavior of a faceted particle to the stable (minimum distortion) configuration. The mesoscale theory was used to model the nematic LC in terms of tensor order parameter $\mathbf{Q}(\mathbf{r})$. Homeotropic anchoring condition of the NLC is imposed on the surfaces of faceted nanoparticles. The results for one particle system suggest that the torque profile is generally divided into two parts: (1) in-plane torques and (2) out-of-plane torques. The magnitude of the out-of-plane torques is similar to that of in-plane torques. However, out-of-plane torque varies more than in-plane torques with respect to the angle of rotation which is evident by their large slope. In case of equilateral triangular prism shaped particle system, the torque reaches maximum when the particle orients with one of its rectangular sides parallel to the far field director $\mathbf{n}(\mathbf{r})$ (i.e. out-of-plane orientations). Whereas, in case of cubic particle, the torque reaches maximum when the particle orients with its four lateral faces parallel to the far field director $\mathbf{n}(\mathbf{r})$ (i.e. out-of-plane orientations). These out-of-plane orientations are unstable configurations and when a particle is oriented at these configurations, it immediately moves away from that state, which is evident by the large slope of the out-of-plane torques, and then it slowly reorients itself to the closest stable configuration (i.e. in-plane orientation). In order to have a zero torque, a configuration should have the highest degree of symmetry along with low NLC distortion around it. The stable

configuration with zero torque was observed for both cubic and triangular prism particle around all the other axes except when a cubic particle is oriented along $z=0$, $x=y$ axis. The torque transmitted by the NLC on a triangular prism shaped particle (Figure 2.3) is nearly twice than that on a cubic particle (Figure 2.8, 2.10, and 2.12), due to the size effect. Thus, a stronger driving force is required to reorient triangular prism shaped particles back to the same stable configurations as compared to cubic particles under the possible switching condition with the ratio of size of nanocube and nanoprism similar to our work. The torque transmitted by the NLC on a cubic particle rotated around the x -axis (Figure 2.14), is nearly five times lower than that on a cubic particle rotated around all the other (Figure 2.8, 2.10 and 2.12) axes due to the axis of rotation affect.

The results for two particles system suggest that, when the two particles are close to each other, the total torque on each triangular prism shaped particle, due to the presence of their respective particle, is nearly twice than that on a cubic particle (Figure 2.6 and 2.16). This difference in the magnitude of the total torque is because of the difference in the trajectory of approach for cubic and triangular prism particles (Figure 2.7 and 2.17). The magnitude of this torques on the particles can be reduced to some extent by making them approach each other via ‘diagonal’ trajectory. Due to the non-spherical shape of the particles, the nematic LC is also expected to transmit force on the particles. Calculation of the forces is not considered in this work and would be the subject of future studies.

In the second part of the research, molecular dynamics simulations of a system of two CNTs immersed in the liquid crystalline solvent were performed in order to investigate how the CNTs interaction are affected by varying the molecular structure and the phase of the LC. Single-walled CNTs with armchair configuration (5, 5) were considered in our simulations. LCs

with different chemical structure: 5CB and 8CB (which are members of the 4-cyano-4'-n-alkylbiphenyl series (nCB)) and different phases: smectic and nematic phase of 8CB LC, were considered in these simulations. The effect of varying the chain length of the hydrophobic tail of the nCB LC molecule on the CNT interactions was investigated by performing the MD simulations of a system of CNTs in 5CB NLCs and CNTs in 8CB NLCs. The results indicate that the CM for 5CB NLCs system is deeper than that of 8CB NLCs system and the PMF for the 5CB NLCs system reaches a value of 0 at larger separation than that of 8CB NLCs system (Figure 3.3). Thus, there is a strong tendency of aggregation for CNTs in the 5CB NLCs system as compared to the 8CB NLCs system. This indicates that, increasing the chain length of the hydrophobic part of the nCB LC molecule decreases the tendency of aggregation for CNTs in nCB LCs.

The effect of varying the phase of the liquid crystalline solvent on the CNTs interactions was investigated by performing the MD simulations of a system of CNTs in 8CB NLCs and CNTs in 8CB SLCs. The results indicate that the CM for 8CB NLCs and SLCs has the same depth and there is a significant difference in the PMF profiles only for small range of separation (Figure 3.5). Thus, the tendency of aggregation for CNTs is similar in both 8CB NLCs and SLCs system. This demonstrates that, varying the phase of the liquid crystalline solvent is insufficient to decrease the tendency of aggregation for CNTs in LCs.

In future, LC molecules with different chemical functionalities such *n*-(4-methoxybenzylidene)-4-butylaniline (MBBA), as well as other trifluorinated bicyclohexyl and cyclohexylbiphenyl derivatives can be considered. Recently, these LC molecules have been commonly used in display applications [133]. The main idea is to see how the LC molecules with different chemical functionalities affect the tendency of aggregation for CNTs in LCs.

Multi-walled CNTs and CNTs with different chirality can also be considered to investigate the tendency of aggregation for CNTs in LCs.

REFERENCES

1. Poulin, P., V. Cabuil, and D.A. Weitz, *Direct Measurement of Colloidal Forces in an Anisotropic Solvent*. Phys. Rev. Lett., 1997. **79**(24): p. 4862-4865.
2. Poulin, P., et al., *Novel colloidal interactions in anisotropic fluids*. Science (Washington, D. C.), 1997. **275**(5307): p. 1770-1773.
3. Poulin, P. and D.A. Weitz, *Inverted and multiple nematic emulsions*. Phys. Rev. E: Stat. Phys., Plasmas, Fluids, Relat. Interdiscip. Top., 1998. **57**(1): p. 626-637.
4. Loudet, J.-C., P. Barois, and P. Poulin, *Colloidal ordering from phase separation in a liquid-crystalline continuous phase*. Nature (London), 2000. **407**(6804): p. 611-613.
5. Nazarenko, V.G., A.B. Nych, and B.I. Lev, *Crystal structure in nematic emulsion*. Phys Rev Lett, 2001. **87**(7): p. 075504.
6. Smalyukh, I.I., et al., *Ordered droplet structures at the liquid crystal surface and elastic-capillary colloidal interactions*. Phys Rev Lett, 2004. **93**(11): p. 117801.
7. Yada, M., J. Yamamoto, and H. Yokoyama, *Spontaneous Formation of Regular Defect Array in Water-in-Cholesteric Liquid Crystal Emulsions*. Langmuir, 2002. **18**(20): p. 7436-7440.
8. Yada, M., J. Yamamoto, and H. Yokoyama, *Direct Observation of Anisotropic Interparticle Forces in Nematic Colloids with Optical Tweezers*. Phys. Rev. Lett., 2004. **92**(18): p. 185501/1-185501/4.
9. Nych, A.B., et al., *Coexistence of two colloidal crystals at the nematic-liquid-crystal-air interface*. Phys Rev Lett, 2007. **98**(5): p. 057801.
10. Ognysta, U., et al., *2D interactions and binary crystals of dipolar and quadrupolar nematic colloids*. Phys Rev Lett, 2008. **100**(21): p. 217803.
11. Kita, K., M. Ichikawa, and Y. Kimura, *Self-assembly of polymer droplets in a nematic liquid crystal at phase separation*. Phys. Rev. E: Stat., Nonlinear, Soft Matter Phys., 2008. **77**(4-1): p. 041702/1-041702/4.
12. Musevic, I., et al., *Two-Dimensional Nematic Colloidal Crystals Self-Assembled by Topological Defects*. Science (Washington, DC, U. S.), 2006. **313**(5789): p. 954-958.
13. Skarabot, M., et al., *Two-dimensional dipolar nematic colloidal crystals*. Phys Rev E Stat Nonlin Soft Matter Phys, 2007. **76**(5 Pt 1): p. 051406.
14. Ravnik, M., et al., *Entangled nematic colloidal dimers and wires*. Phys Rev Lett, 2007. **99**(24): p. 247801.

15. Skarabot, M., et al., *Hierarchical self-assembly of nematic colloidal superstructures*. Phys Rev E Stat Nonlin Soft Matter Phys, 2008. **77**(6 Pt 1): p. 061706.
16. Skarabot, M., et al., *Interactions of quadrupolar nematic colloids*. Phys Rev E Stat Nonlin Soft Matter Phys, 2008. **77**(3 Pt 1): p. 031705.
17. Tkalec, U., M. Skarabot, and I. Musevic, *Interactions of micro-rods in a thin layer of a nematic liquid crystal*. Soft Matter, 2008. **4**(12): p. 2402-2409.
18. Takahashi, K., M. Ichikawa, and Y. Kimura, *Force between colloidal particles in a nematic liquid crystal studied by optical tweezers*. Phys. Rev. E: Stat., Nonlinear, Soft Matter Phys., 2008. **77**(2-1): p. 020703/1-020703/4.
19. Guzman, O., et al., *Defect structure around two colloids in a liquid crystal*. Phys Rev Lett, 2003. **91**(23): p. 235507.
20. Grollau, S., et al., *Monte Carlo simulations and dynamic field theory for suspended particles in liquid crystalline systems*. J. Chem. Phys., 2003. **119**(4): p. 2444-2455.
21. Kim, E.B., et al., *Interactions between spherical colloids mediated by a liquid crystal: a molecular simulation and mesoscale study*. J. Chem. Phys., 2004. **121**(4): p. 1949-1961.
22. Guzman, O., N.L. Abbott, and P.J.J. De, *Defect structures and three-body potential of the mean force for nanoparticles in a nematic host*. J. Polym. Sci., Part B: Polym. Phys., 2005. **43**(8): p. 1033-1040.
23. Hung, F.R., et al., *Anisotropic nanoparticles immersed in a nematic liquid crystal: Defect structures and potentials of mean force*. Phys. Rev. E: Stat., Nonlinear, Soft Matter Phys., 2006. **74**(1-1): p. 011711/1-011711/12.
24. Hung, F.R., et al., *Nanoparticles in nematic liquid crystals: interactions with nanochannels*. J. Chem. Phys., 2007. **127**(12): p. 124702/1-124702/10.
25. Qi, H. and T. Hegmann, *Formation of periodic stripe patterns in nematic liquid crystals doped with functionalized gold nanoparticles*. J. Mater. Chem., 2006. **16**(43): p. 4197-4205.
26. Qi, H., et al., *Effects of hydrophilic and hydrophobic gold nanoclusters on the stability and ordering of bolaamphiphilic liquid crystals*. J. Mater. Chem., 2007. **17**(20): p. 2139-2144.
27. Mitov, M., C. Bourgerette, and G.F. De, *Fingerprint patterning of solid nanoparticles embedded in a cholesteric liquid crystal*. J. Phys.: Condens. Matter, 2004. **16**(19): p. S1981-S1988.
28. Van, B.M.C.W., et al., *Polymer-filled nematics: a new class of light-scattering materials for electro-optical switches*. Adv. Mater. (Weinheim, Ger.), 2000. **12**(10): p. 753-757.

29. Nersisyan, S.R. and N.V. Tabiryan, *The effect of low-frequency microvibrations on nanoparticle networks embedded in liquid crystals*. Appl. Phys. Lett., 2006. **88**(15): p. 151106/1-151106/3.
30. Kossyrev, P.A., et al., *Electric Field Tuning of Plasmonic Response of Nanodot Array in Liquid Crystal Matrix*. Nano Lett., 2005. **5**(10): p. 1978-1981.
31. Hegmann, T., H. Qi, and V.M. Marx, *Nanoparticles in liquid crystals: synthesis, self-assembly, defect formation and potential applications*. J. Inorg. Organomet. Polym. Mater., 2007. **17**(3): p. 483-508.
32. Qi, H. and T. Hegmann, *Impact of nanoscale particles and carbon nanotubes on current and future generations of liquid crystal displays*. J. Mater. Chem., 2008. **18**(28): p. 3288-3294.
33. Lapointe, C., et al., *Elastic Torque and the Levitation of Metal Wires by a Nematic Liquid Crystal*. Science (Washington, DC, U. S.), 2004. **303**(5658): p. 652-655.
34. Lynch, M.D. and D.L. Patrick, *Organizing Carbon Nanotubes with Liquid Crystals*. Nano Lett., 2002. **2**(11): p. 1197-1201.
35. Lynch, M.D. and D.L. Patrick, *Controlling the Orientation of Micron-Sized Rod-Shaped SiC Particles with Nematic Liquid Crystal Solvents*. Chem. Mater., 2004. **16**(5): p. 762-767.
36. Dierking, I., et al., *Aligning and reorienting carbon nanotubes with nematic liquid crystals*. Adv. Mater. (Weinheim, Ger.), 2004. **16**(11): p. 865-869.
37. van, d.S.P., V. Popa-Nita, and S. Kralj, *Alignment of Carbon Nanotubes in Nematic Liquid Crystals*. J. Phys. Chem. B, 2008. **112**(15): p. 4512-4518.
38. Available from: http://barrett-group.mcgill.ca/teaching/liquid_crystal.
39. Gupta, V.K., et al., *Optical amplification of ligand-receptor binding using liquid crystals*. Science (Washington, D. C.), 1998. **279**(5359): p. 2077-2080.
40. Shah, R.R. and N.L. Abbott, *Principles for measurement of chemical exposure based on recognition-driven anchoring transitions in liquid crystals*. Science (Washington, DC, U. S.), 2001. **293**(5533): p. 1296-1299.
41. Brake, J.M., et al., *Biomolecular Interactions at Phospholipid-Decorated Surfaces of Liquid Crystals*. Science (Washington, DC, U. S.), 2003. **302**(5653): p. 2094-2098.
42. Koenig, G.M., Jr., et al., *Coupling of the Plasmon Resonances of Chemically Functionalized Gold Nanoparticles to Local Order in Thermotropic Liquid Crystals*. Chem. Mater., 2007. **19**(5): p. 1053-1061.

43. Koenig, G.M., Jr., et al., *Using Localized Surface Plasmon Resonances to Probe the Nanoscopic Origins of Adsorbate-Driven Ordering Transitions of Liquid Crystals in Contact with Chemically Functionalized Gold Nanodots*. Nano Lett., 2008. **8**(8): p. 2362-2368.
44. Tjipto, E., et al., *Tailoring the Interfaces between Nematic Liquid Crystal Emulsions and Aqueous Phases via Layer-by-Layer Assembly*. Nano Lett., 2006. **6**(10): p. 2243-2248.
45. Shiyakovskii, S.V., et al., *Real-time microbe detection based on director distortions around growing immune complexes in lyotropic chromonic liquid crystals*. Phys Rev E Stat Nonlin Soft Matter Phys, 2005. **71**(2 Pt 1): p. 020702.
46. Muller, J., et al., *Electrically controlled light scattering with single metal nanoparticles*. Appl. Phys. Lett., 2002. **81**(1): p. 171-173.
47. Grollau, S., et al., *Slow dynamics of thin nematic films in the presence of adsorbed nanoparticles*. J Chem Phys, 2005. **122**(2): p. 024703.
48. Guzman, O., N.L. Abbott, and P.J.J. de, *Quenched disorder in a liquid-crystal biosensor: adsorbed nanoparticles at confining walls*. J Chem Phys, 2005. **122**(18): p. 184711.
49. Hwang, D.K. and A.D. Rey, *Optical modeling of liquid crystal biosensors*. J. Chem. Phys., 2006. **125**(17): p. 174902/1-174902/9.
50. Mohanraj, R. and H. Wu, *Simulation of dynamics of a nematic liquid crystal for a biosensor application*. Sens. Lett., 2007. **5**(3/4): p. 538-551.
51. de, G.P.G. and J. Prost, *The Physics of Liquid Crystals, Second Edition* 1993: Oxford Univ. Press. 597 pp.
52. Stark, H., *Physics of colloidal dispersions in nematic liquid crystals*. Phys. Rep., 2001. **351**(6): p. 387-474.
53. Mondain-Monval, O., et al., *Weak surface energy in nematic dispersions: Saturn ring defects and quadrupolar interactions*. Eur. Phys. J. B, 1999. **12**(2): p. 167-170.
54. Gu, Y. and N.L. Abbott, *Observation of Saturn-Ring Defects around Solid Microspheres in Nematic Liquid Crystals*. Phys. Rev. Lett., 2000. **85**(22): p. 4719-4722.
55. Ruhwandl, R.W. and E.M. Terentjev, *Long-range forces and aggregation of colloid particles in a nematic liquid crystal*. Phys. Rev. E: Stat. Phys., Plasmas, Fluids, Relat. Interdiscip. Top., 1997. **55**(3-A): p. 2958-2961.
56. Ruhwandl, R.W. and E.M. Terentjev, *Monte Carlo simulation of topological defects in the nematic liquid crystal matrix around a spherical colloid particle*. Phys. Rev. E: Stat. Phys., Plasmas, Fluids, Relat. Interdiscip. Top., 1997. **56**(5-B): p. 5561-5565.

57. Lubensky, T.C., et al., *Topological defects and interactions in nematic emulsions*. Phys. Rev. E: Stat. Phys., Plasmas, Fluids, Relat. Interdiscip. Top., 1998. **57**(1): p. 610-625.
58. Stark, H., *Director field configurations around a spherical particle in a nematic liquid crystal*. Eur. Phys. J. B, 1999. **10**(2): p. 311-321.
59. Fukuda, J.-i., M. Yoneya, and H. Yokoyama, *Nematic liquid crystal around a spherical particle: investigation of the defect structure and its stability using adaptive mesh refinement*. Eur. Phys. J. E, 2004. **13**(1): p. 87-98.
60. Al-Barwani, M.S., G.S. Sutcliffe, and M.P. Allen, *Forces between Two Colloidal Particles in a Nematic Solvent*. J. Phys. Chem. B, 2004. **108**(21): p. 6663-6666.
61. De, L.G. and A.D. Rey, *Point and ring defects in nematics under capillary confinement*. J Chem Phys, 2007. **127**(10): p. 104902.
62. De, L.G. and A.D. Rey, *Ringlike cores of cylindrically confined nematic point defects*. J Chem Phys, 2007. **126**(9): p. 094907.
63. Skacej, G. and C. Zannoni, *Controlling surface defect valence in colloids*. Phys Rev Lett, 2008. **100**(19): p. 197802.
64. Voltz, C., et al., *Director-configurational transitions around microbubbles of hydrostatically regulated size in liquid crystals*. Phys Rev Lett, 2006. **97**(22): p. 227801.
65. Loudet, J.C. and P. Poulin, *Application of an electric field to colloidal particles suspended in a liquid-crystal solvent*. Phys Rev Lett, 2001. **87**(16): p. 165503.
66. Grollau, S., N.L. Abbott, and P.J.J. de, *Spherical particle immersed in a nematic liquid crystal: effects of confinement on the director field configurations*. Phys Rev E Stat Nonlin Soft Matter Phys, 2003. **67**(1 Pt 1): p. 011702.
67. Fukuda, J.-I., et al., *Interaction between two spherical particles in a nematic liquid crystal*. Phys. Rev. E: Stat., Nonlinear, Soft Matter Phys., 2004. **69**(4-1): p. 041706/1-041706/10.
68. Fukuda, J.-I. and H. Yokoyama, *Separation-independent attractive force between like particles mediated by nematic-liquid-crystal distortions*. Phys Rev Lett, 2005. **94**(14): p. 148301.
69. Hung, F.R., *Quadrupolar particles in a nematic liquid crystal: Effects of particle size and shape*. Phys. Rev. E: Stat., Nonlinear, Soft Matter Phys., 2009. **79**(2-1): p. 021705/1-021705/11.
70. Cheung, D.L. and M.P. Allen, *Structure of a liquid crystalline fluid around a macroparticle: Density functional theory*. Phys. Rev. E: Stat., Nonlinear, Soft Matter Phys., 2006. **74**(2-1): p. 021701/1-021701/8.

71. Cheung, D.L. and M.P. Allen, *Forces between Cylindrical Nanoparticles in a Liquid Crystal*. Langmuir, 2008. **24**(4): p. 1411-1417.
72. Cheung, D.L. and M.P. Allen, *Effect of substrate geometry on liquid-crystal-mediated nanocylinder-substrate interactions*. J. Chem. Phys., 2008. **129**(11): p. 114706/1-114706/7.
73. Yamamoto, R., *Simulating particle dispersions in nematic liquid-crystal solvents*. Phys Rev Lett, 2001. **87**(7): p. 075502.
74. Yamamoto, R., Y. Nakayama, and K. Kim, *A smooth interface method for simulating liquid crystal colloid dispersions*. J. Phys.: Condens. Matter, 2004. **16**(19): p. S1945-S1955.
75. Araki, T. and H. Tanaka, *Colloidal Aggregation in a Nematic Liquid Crystal: Topological Arrest of Particles by a Single-Stroke Disclination Line*. Phys. Rev. Lett., 2006. **97**(12): p. 127801/1-127801/4.
76. Sulaiman, N., D. Marenduzzo, and J.M. Yeomans, *Lattice Boltzmann algorithm to simulate isotropic-nematic emulsions*. Phys Rev E Stat Nonlin Soft Matter Phys, 2006. **74**(4 Pt 1): p. 041708.
77. Zhou, C., P. Yue, and J.J. Feng, *Dynamic Simulation of Droplet Interaction and Self-Assembly in a Nematic Liquid Crystal*. Langmuir, 2008. **24**(7): p. 3099-3110.
78. Xu, J., et al., *Molecular dynamics simulation study of spherical nanoparticles in a nematogenic matrix. Anchoring, interactions, and phase behavior*. Phys. Rev. E: Stat., Nonlinear, Soft Matter Phys., 2009. **79**(1-1): p. 011704/1-011704/12.
79. Ravnik, M. and S. Zumer, *Nematic braids: 2D entangled nematic liquid crystal colloids*. Soft Matter, 2009. **5**(22): p. 4520-4525.
80. Skarabot, M. and I. Musevic, *Direct observation of interaction of nanoparticles in a nematic liquid crystal*. Soft Matter. **6**(21): p. 5476-5481.
81. Phillips, P.M., et al., *Textures in Polygonal Arrangements of Square Nanoparticles in Nematic Liquid Crystal Matrices*. Langmuir. **27**(21): p. 13335-13341.
82. Koenig, G.M., Jr., P.J.J. de, and N.L. Abbott, *Characterization of the Reversible Interaction of Pairs of Nanoparticles Dispersed in Nematic Liquid Crystals*. Langmuir, 2009. **25**(23): p. 13318-13321.
83. Dontabhaktuni, J., M. Ravnik, and S. Zumer, *Shape-tuning the colloidal assemblies in nematic liquid crystals*. Soft Matter, 2012. **8**(Copyright (C) 2012 American Chemical Society (ACS). All Rights Reserved.): p. 1657-1663.

84. Lapointe, C.P., et al., *Electrically Driven Multiaxis Rotational Dynamics of Colloidal Platelets in Nematic Liquid Crystals*. Phys. Rev. Lett., 2010. **105**(Copyright (C) 2012 American Chemical Society (ACS). All Rights Reserved.): p. 178301/1-178301/4.
85. Lagerwall, J.P.F. and G. Scalia, *Carbon nanotubes in liquid crystals*. J. Mater. Chem., 2008. **18**(25): p. 2890-2898.
86. Patrick, D.L., F.S. Wilkinson, and T.L. Fegurgur, *Getting organized at the nanoscale with thermotropic liquid crystal solvents*. Proc. SPIE-Int. Soc. Opt. Eng., 2005. **5936**(Liquid Crystals IX): p. 59360A/1-59360A/8.
87. Zakri, C., *Carbon nanotubes and liquid crystalline phases*. Liq. Cryst. Today, 2007. **16**(1): p. 1-11.
88. Lapointe, C.P., D.H. Reich, and R.L. Leheny, *Manipulation and Organization of Ferromagnetic Nanowires by Patterned Nematic Liquid Crystals*. Langmuir, 2008. **24**(19): p. 11175-11181.
89. Iijima, S., *Helical microtubules of graphitic carbon*. Nature (London), 1991. **354**(6348): p. 56-8.
90. Saito, R., et al., *Physics of Carbon Nanotube* 1998: World Sci. 200 pp. (approx.).
91. Bandosz, T.J., et al., *Molecular models of porous carbons*. Chem. Phys. Carbon, 2003. **28**: p. 41-228.
92. Chen, H.-Y., W. Lee, and N.A. Clark, *Faster electro-optical response characteristics of a carbon-nanotube nematic suspension*. Appl. Phys. Lett., 2007. **90**(3): p. 033510/1-033510/3.
93. Jeon, S.Y., et al., *Effects of carbon nanotubes on electrooptical characteristics of liquid crystal cell driven by in-plane field*. Appl. Phys. Lett., 2007. **90**(12): p. 121901/1-121901/3.
94. Qi, H., B. Kinkead, and T. Hegmann, *Effects of functionalized metal and semiconductor nanoparticles in nematic liquid crystal phases*. Proc. SPIE, 2008. **6911**(Emerging Liquid Crystal Technologies III): p. 691106/1-691106/11.
95. Uddin, N.M., F.M. Capaldi, and B. Farouk, *Molecular dynamics simulations of the interactions and dispersion of carbon nanotubes in polyethylene oxide/water systems*. Polymer. **52**(2): p. 288-296.
96. Tummala, N.R., et al., *Stabilization of aqueous carbon nanotube dispersions using surfactants: insights from molecular dynamics simulations*. ACS Nano. **4**(12): p. 7193-204.
97. Suttipong, M., et al., *Role of Surfactant Molecular Structure on Self-Assembly: Aqueous SDBS on Carbon Nanotubes*. J. Phys. Chem. C. **115**(35): p. 17286-17296.

98. Lin, S. and D. Blankschtein, *Role of the Bile Salt Surfactant Sodium Cholate in Enhancing the Aqueous Dispersion Stability of Single-Walled Carbon Nanotubes: A Molecular Dynamics Simulation Study*. J. Phys. Chem. B. **114**(47): p. 15616-15625.
99. Puech, N., et al., *Highly Ordered Carbon Nanotube Nematic Liquid Crystals*. J. Phys. Chem. C. **115**(8): p. 3272-3278.
100. Glotzer, S.C., *Materials science: Some assembly required*. Science (Washington, DC, U. S.), 2004. **306**(5695): p. 419-420.
101. Glotzer, S.C. and M.J. Solomon, *Anisotropy of building blocks and their assembly into complex structures*. Nat Mater, 2007. **6**(8): p. 557-62.
102. Velev, O.D., *Self-Assembly of Unusual Nanoparticle Crystals*. Science (Washington, DC, U. S.), 2006. **312**(5772): p. 376-377.
103. Gangwal, S., O.J. Cayre, and O.D. Velev, *Dielectrophoretic Assembly of Metallodielectric Janus Particles in AC Electric Fields*. Langmuir, 2008. **24**(23): p. 13312-13320.
104. Shevchenko, E.V., et al., *Structural diversity in binary nanoparticle superlattices*. Nature (London, U. K.), 2006. **439**(7072): p. 55-59.
105. Kalsin, A.M., et al., *Electrostatic Self-Assembly of Binary Nanoparticle Crystals with a Diamond-Like Lattice*. Science (Washington, DC, U. S.), 2006. **312**(5772): p. 420-424.
106. Stebe, K.J., E. Lewandowski, and M. Ghosh, *Materials science. Oriented assembly of metamaterials*. Science, 2009. **325**(5937): p. 159-60.
107. Sun, Y. and Y. Xia, *Shape-Controlled Synthesis of Gold and Silver Nanoparticles*. Science (Washington, DC, U. S.), 2002. **298**(5601): p. 2176-2179.
108. Cho, K.-S., et al., *Designing PbSe Nanowires and Nanorings through Oriented Attachment of Nanoparticles*. J. Am. Chem. Soc., 2005. **127**(19): p. 7140-7147.
109. Dendukuri, D., et al., *Continuous-flow lithography for high-throughput microparticle synthesis*. Nat. Mater., 2006. **5**(5): p. 365-369.
110. Malikova, N., et al., *Layer-by-Layer Assembled Mixed Spherical and Planar Gold Nanoparticles: Control of Interparticle Interactions*. Langmuir, 2002. **18**(9): p. 3694-3697.
111. Hung, F.R. and S. Bale, *Faceted nanoparticles in a nematic liquid crystal: defect structures and potentials of mean force*. Mol. Simul., 2009. **35**(10-11): p. 822-834; Available from: <http://www.tandfonline.com>.

112. Gupta, V.K. and N.L. Abbott, *Design of surfaces for patterned alignment of liquid crystals on planar and curved substrates*. Science (Washington, D. C.), 1997. **276**(5318): p. 1533-1536.
113. Beris, A.N., *Thermodynamics of Flowing Systems with Internal Microstructure* 1994: Oxford University Press, New York
114. Edwards, B.J. and A.N. Beris, *Order parameter representation of spatial inhomogeneities in polymeric liquid crystals*. J. Rheol. (N. Y.), 1989. **33**(7): p. 1189-93.
115. Edwards, B.J., A.N. Beris, and M. Grmela, *Generalized constitutive equation for polymeric liquid crystals. Part 1. Model formulation using the Hamiltonian (Poisson bracket) formulation*. J. Non-Newtonian Fluid Mech., 1990. **35**(1): p. 51-72.
116. Schopohl, N., Phys Rev Lett, 1987. **59**.
117. *COMSOL Multiphysics™ Version 3.4 User's Guide* 2007, Burlington, MA: COMSOL, Inc., .
118. *For the case of Equation (6), the elastic term and the Landau-de Gennes terms were included as part of the diffusive flux (c) and source (f) terms, respectively, of the coefficient PDE form of COMSOL Multiphysics™. The models were created, executed and saved as a MATLAB® M-file.*
119. Kralj, S., E.G. Virga, and S. Zumer, *Biaxial torus around nematic point defects*. Phys. Rev. E: Stat. Phys., Plasmas, Fluids, Relat. Interdiscip. Top., 1999. **60**(2-B): p. 1858-1866.
120. Callan-Jones, A.C., et al., *Simulation and visualization of topological defects in nematic liquid crystals*. Phys Rev E Stat Nonlin Soft Matter Phys, 2006. **74**(6 Pt 1): p. 061701.
121. Kralj, S., J. Phys. A: Math. Gen., 2001. **34**.
122. Kralj, S. and E.G. Virga, *Core hysteresis in nematic defects*. Phys Rev E Stat Nonlin Soft Matter Phys, 2002. **66**(Copyright (C) 2012 U.S. National Library of Medicine.): p. 021703.
123. McKay, G. and E.G. Virga, *Mechanical actions on nanocylinders in nematic liquid crystals*. Phys. Rev. E: Stat., Nonlinear, Soft Matter Phys., 2005. **71**(4-1): p. 041702/1-041702/11.
124. Hess, B., et al., *GROMACS 4: Algorithms for Highly Efficient, Load-Balanced, and Scalable Molecular Simulation*. J. Chem. Theory Comput., 2008. **4**(3): p. 435-447.
125. Schuettelkopf, A.W. and A.D.M.F. van, *PRODRG: a tool for high-throughput crystallography of protein-ligand complexes*. Acta Crystallogr., Sect. D: Biol. Crystallogr., 2004. **D60**(8): p. 1355-1363.

126. *Nanotube Modeler Version 1.7.1, JCrystalSoft (2005); and references therein.*
127. Humphrey, W., A. Dalke, and K. Schulten, *VMD: Visual molecular dynamics*. Journal of Molecular Graphics, 1996. **14**(1): p. 33-38.
128. Tiberio, G., et al., *Towards in Silico liquid crystals. Realistic transition temperatures and physical properties for n-cyanobiphenyls via molecular dynamics simulations*. ChemPhysChem, 2009. **10**(1): p. 125-136.
129. Dang, L.X., *Computational Study of Ion Binding to the Liquid Interface of Water*. J. Phys. Chem. B, 2002. **106**(40): p. 10388-10394.
130. Trzesniak, D., A.-P.E. Kunz, and G.W.F. van, *A comparison of methods to compute the potential of mean force*. ChemPhysChem, 2007. **8**(1): p. 162-169.
131. Mastny, E.A., C.A. Miller, and P.J.J. de, *The effect of the water/methane interface on methane hydrate cages: The potential of mean force and cage lifetimes*. J. Chem. Phys., 2008. **129**(3): p. 034701/1-034701/8.
132. Miller, C.A., N.L. Abbott, and P.J.J. de, *Surface Activity of Amphiphilic Helical \hat{I}^2 -Peptides from Molecular Dynamics Simulation*. Langmuir, 2009. **25**(5): p. 2811-2823.
133. Deschamps, J., J.P.M. Trusler, and G. Jackson, *Vapor Pressure and Density of Thermotropic Liquid Crystals: MBBA, 5CB, and Novel Fluorinated Mesogens*. The Journal of Physical Chemistry B, 2008. **112**(13): p. 3918-3926.

APPENDIX A

Molecular Simulation
Vol. 35, Nos. 10–11, September 2009, 822–834



Faceted nanoparticles in a nematic liquid crystal: defect structures and potentials of mean force

Francisco R. Hung* and Shivkumar Bale

Cain Department of Chemical Engineering, Louisiana State University, Baton Rouge, LA 70803, USA

(Received 23 December 2008; final version received 30 January 2009)

We investigate the defect structures and the potentials of mean force (PMF) that arise when faceted nanoparticles, namely cubes and triangular prisms, are immersed in a nematic liquid crystal (NLC). Using a mesoscale theory for the tensor order parameter \mathbf{Q} of the nematic, we have determined the thermodynamic stability of different orientations of one nanoparticle with respect to the far-field director $\mathbf{n}(\mathbf{r})$. A nanocube with perpendicular anchoring of the nematic at its surfaces tends to align in such a way that none of its faces is parallel or perpendicular to $\mathbf{n}(\mathbf{r})$; the most stable defect structure consists of a distorted Saturn ring with sharp bends, which covers six of the edges of the cubic particle. In contrast, a triangular nanoprism with homeotropic anchoring of the nematic at its surfaces tends to align with its long axis perpendicular to the far-field director $\mathbf{n}(\mathbf{r})$, and with one of its rectangular faces perpendicular to $\mathbf{n}(\mathbf{r})$. For such a configuration, the defect structure consists of two large disclination regions covering the two triangular faces of the prism, and two narrow disclination regions surrounding two of the rounded edges of the prism. We also studied the thermodynamic stability of different arrays of two particles, finding that for two nanocubes that approach each other keeping their orientations fixed, the nematic forms a distorted 'entangled hyperbolic' defect structure around the particles, in analogy to what was observed for pairs of spherical and spherocylindrical nanoparticles in close proximity. The NLC-mediated interactions between the nanocubes in this case are of the order of $-85k_B T$, which are weaker than those observed for spherical nanoparticles of comparable diameter ($\sim -110k_B T$). For systems of two nanoprisms having their long axes perpendicular to the far-field director, we considered three particle arrays: linear (the long axes of the particles are collinear and the particles have the same orientation), parallel (the long axes of the particles are parallel and the particles have the same orientation) and inverted parallel (the long axes of the particles are parallel, and one of the prisms is inverted with respect to the other one). Our results suggest that inverted parallel arrays are thermodynamically more stable than linear arrays, which in turn are more stable than parallel arrays. The minima observed in the PMF curves for the inverted parallel ($\sim -1050k_B T$) and linear arrays ($\sim -525k_B T$) are significantly deeper than that observed for the parallel array ($\sim -150k_B T$). In comparison, a pair of nanospheres with a diameter comparable to the size of the triangular faces of our nanoprisms has a PMF minimum of $\sim 73k_B T$ when the spheres are in close proximity. These NLC-mediated, anisotropic interparticle interactions can make the particles bind together at specific locations, and thus could be used to assemble the particles into ordered structures with different morphologies.

Keywords: nanocubes; nanoprisms; nematic liquid crystal; mesoscale theory; simulation

APPENDIX B



Shivkumar Bale <sbale1@tigers.lsu.edu>

FW: Permissions to use my paper into my thesis

1 message

Beesley, Karin <Karin.Beesley@tandf.co.uk>
To: sbale1@tigers.lsu.edu

Mon, Apr 23, 2012 at 4:25 AM

Our Ref: KB/GMOS/P6534

23rd April 2012

Dear Shivkumar Bale

Thank you for your correspondence requesting permission to reproduce the following material from our Journal in your thesis:

Faceted nanoparticles in a nematic liquid crystal: defect structures and potentials of mean force – vol 35 no 10-11 2009 pp 822-834

We will be pleased to grant entirely free permission on the condition that you acknowledge the original source of publication and insert a reference to the Journal's web site:

<http://www.tandfonline.com>

Thank you for your interest in our Journal.

Yours sincerely

Karin Beesley

Permissions Administrator

Taylor & Francis Group

Taylor & Francis Group is a trading name of Informa UK Limited, registered in England under no. 1072954

From: Shivkumar Bale [mailto:sbale1@tigers.lsu.edu]

Sent: Wednesday, March 07, 2012 5:18 PM

To: phrlpermissions

Subject: Permissions to use my paper into my thesis

Dear Permissions Manager,

My name is Shivkumar Bale. I want to use the figures from my paper into my thesis. The details of the paper are as follows:

Title: Faceted nanoparticles in a nematic liquid crystal: defect structures and potentials of mean force

Author: Francisco Hung, Shivkumar Bale

Publication: Molecular Simulation

Publisher: Taylor & Francis

Date: Sept 1, 2009

Thanks

--

Shivkumar Bale
Doctoral Student
Cain Department of Chemical Engineering
Louisiana State University
Baton Rouge, LA 70803
Phone: (225) 614-1476
Email: sbale1@tigers.lsu.edu

The information contained in this email message may be confidential. If you are not the intended recipient, any use, interference with, disclosure or copying of this material is unauthorised and prohibited. Although this message and any attachments are believed to be free of viruses, no responsibility is accepted by Informa for any loss or damage arising in any way from receipt or use thereof. Messages to and from the company are monitored for operational reasons and in accordance with lawful business practices.

If you have received this message in error, please notify us by return and delete the message and any attachments. Further enquiries/returns can be sent to postmaster@informa.com

Taylor & Francis Group is a trading name of Informa UK Limited, registered in England under no. 1072954

VITA

Shivkumar Shankar Bale was born in Mumbai, India, on October 1984. After completing his high school and secondary college, he graduated from Mumbai University Institute of Chemical Technology, India, with a Bachelor degree in Chemical Technology on June 2006. After working at Goderj Industries Limited, Mumbai, as a production officer for a year, Shivkumar was admitted into the Graduate program of the Department of Chemical Engineering at Louisiana State University, Baton Rouge, on August 2007. Under the guidance of Dr. Francisco Hung at Louisiana State University for the Doctor of Philosophy degree in Chemical Engineering, he worked on computer simulations of faceted nanoparticles and carbon nanotubes in liquid crystals. He plans to graduate with a Doctorate degree at the summer 2012 commencement.